Accessibility of the unstructured α-tubulin C-terminal tail is controlled by microtubule lattice conformation

Takashi Hotta[1]*, Morgan L. Pimm[1]*, Ezekiel C. Thomas[1]*, Yang Yue[1]*, Patrick DeLear[2,3], Lynne Blasius[1], Michael Cianfrocco[4], Morgan DeSantis[5], Ryota Horiuchi[6], Takumi Higaki[6,7], David Sept[3], Ryoma Ohi[1#], and Kristen J. Verhey[1,2#]

[1]Department of Cell & Developmental Biology, University of Michigan, Ann Arbor, MI, USA
[2]Department of Biophysics, University of Michigan, Ann Arbor, MI, USA
[3]Department of Biomedical Engineering, University of Michigan, Ann Arbor, MI, USA
[4]Department of Biological Chemistry, University of Michigan, Ann Arbor, MI, USA
[5]Department of Molecular, Cellular and Developmental Biology, University of Michigan, Ann Arbor, MI, USA
[6]Graduate School of Science and Technology, Kumamoto University, Kumamoto, Japan
[7]International Research Organization for Advanced Science and Technology, Kumamoto University, Kumamoto, Japan

*these authors contributed equally to this work.
[#]corresponding authors: oryoma@umich.edu, kjverhey@umich.edu

T Hotta and R Ohi current address: Department of Internal Medicine, University of New Mexico Comprehensive Cancer Center, Albuquerque, New Mexico

Impact statement: Using three different biosensors, the authors determine that the C-terminal tail of α-tubulin does not freely extend from the microtubule surface as widely thought, but rather is inaccessible along most microtubules in cells.

ABSTRACT

Microtubules are cytoskeletal filaments that self-assemble from the protein tubulin, a heterodimer of α-tubulin and β-tubulin, and are important for cell mechanics, migration, and division. Much work has focused on how the nucleotide state of β-tubulin regulates the structure and dynamics of microtubules. In contrast, less is known about the structure and function of the C-terminal tails (CTTs) of α- and β-tubulin which are thought to freely protrude from the surface of the microtubule. To study the CTT of α-tubulin, we developed three different biosensors that bind the tyrosinated α-tubulin CTT (Y-αCTT). Surprisingly, live imaging of the probes indicates that the Y-αCTT is minimally accessible along the microtubule lattice under normal cellular conditions. Lattice binding of the Y-αCTT probes can be increased by three different ways of changing the tubulin conformational state: the drug Taxol, expression of microtubule-associated proteins (MAPs) that recognize or promote an expanded tubulin conformation, or expression of tubulin that cannot hydrolyze GTP. Molecular dynamics simulations indicate that the Y-αCTT undergoes numerous transient interactions with the bodies of α-tubulin and β-tubulin in the lattice, and that the frequency of these interactions is regulated by the tubulin nucleotide state. These findings suggest that accessibility of the Y-αCTT is locally governed by nucleotide- and MAP-dependent conformational changes to tubulin subunits within the microtubule lattice.

INTRODUCTION

Microtubules are dynamic polymers that provide mechanical support to cells, serve as tracks for intracellular trafficking, and form the mitotic spindle that separates the replicated genome during cell division (Forth & Kapoor, 2017; Fourriere et al., 2020; Logan & Menko, 2019; Prosser & Pelletier, 2017; Risteski et al., 2021). Microtubules are formed by self-assembly of the protein tubulin, a heterodimer of α-tubulin and β-tubulin. Although both α- and β-tubulin bind GTP and thus belong to the superfamily of G proteins (Hughes, 1983; Nogales et al., 1998), only β-tubulin hydrolyzes GTP and exchanges GDP for GTP.

The ability of β-tubulin to hydrolyze GTP is intimately linked to microtubule assembly and disassembly (Chew & Cross, 2025; Cleary & Hancock, 2021; Gudimchuk & McIntosh, 2021). During polymerization, tubulin subunits with GTP bound to β-tubulin (GTP-tubulin) associate in a head-to-tail fashion with the plus (growing) end of the microtubule. After incorporation into the microtubule lattice, β-tubulin hydrolyzes its GTP to GDP. When GDP-tubulin subunits are exposed at the plus end, microtubules are unstable and depolymerization ensues. Thus, a cap of GTP-tubulin stabilizes the microtubule lattice (Mitchison & Kirschner, 1984) (**Figure 1A,B**).

Recent work suggests that GTP hydrolysis by β-tubulin triggers a decrease in the spacing of tubulin subunits along the longitudinal axis of the microtubule, largely due to conformational changes in the associated α-tubulin subunit. Specifically, cryo-electron microscopy (cryo-EM) of microtubules assembled *in vitro* show GTP- or GTP-like tubulin to be in an expanded state (dimer length 83-84 Å) whereas GDP-Pi or GDP-tubulin is in a compacted state (dimer length 81-82 Å) (Alushin et al., 2014; Estevez-Gallego et al., 2025; Estevez-Gallego et al., 2020; LaFrance et al., 2022; Manka & Moores, 2018; Zhang et al., 2018) (**Figure 1B**). In cells, most microtubules have a compacted lattice (dimer length ~82 Å), consistent with their being in the GDP state (de Jager et al., 2025).

GDP-tubulin subunits within the lattice can be switched from their compacted state to a GTP-like expanded state by tubulin-binding drugs and microtubule associated proteins (MAPs). Taxol is a natural product that stabilizes microtubules and cryo-EM studies showed that Taxol expands the microtubule lattice *in vitro* (dimer length ~84Å) and in cells (dimer length ~85Å) (Alushin et al., 2014; de Jager et al., 2025; Kellogg et al., 2017; Prota et al., 2023). MAP binding can also alter tubulin conformational state although in these studies, the lattice state has largely been deduced from light microscopy experiments and thus the exact changes in dimer length are unclear. The MAPs kinesin-1 and CAMSAP3 recognize and/or induce an expanded microtubule lattice (de Jager et al., 2025; Liu & Shima, 2023; Peet et al., 2018; Shen & Ori-McKenney, 2024; Shima et al., 2018) whereas the MAPs tau, MAP2, and doublecortin (DCX) recognize and/or induce a compacted microtubule lattice (Castle et al., 2020; Paquette et al., 2025; Siahaan et al., 2022). In cells, microtubule lattice conformation can also be altered upon changes in the osmotic environment (Shen & Ori-McKenney, 2024). At least three outcomes have been linked to conformational plasticity of tubulin subunits within the lattice (Chew & Cross, 2025; Verhey & Ohi, 2023). First, tubulin isotypes may differ in their ability to undergo compaction and expansion and thereby impact cell- and tissue-specific responses to drugs and MAPs (Chew & Cross, 2023; Howes et al., 2017). Second, molecular motor proteins that step along the microtubule surface can communicate with each other through the lattice (Muto et al., 2005; Wijeratne et al., 2022). Third, microtubule lattice state regulates the tubulin code by

permitting specific subsets of microtubules to be marked by tubulin post-translational modifications (PTMs) (Egoldt et al., 2025; Shen & Ori-McKenney, 2024; Yue et al., 2023; Yue et al., 2025).

A critical element of both α- and β-tubulins is their C-terminal tails (CTTs) (**Figure 1A**), disordered and negatively-charged segments that extend from the body of the tubulin proteins. The CTTs alter microtubule dynamics by impeding microtubule polymerization and increasing the growth-to-shortening transition (Serrano, de la Torre, et al., 1984). The CTTs are thought to be a major control hub of the microtubule lattice as they contain the majority of sequence differences between tubulin isotypes and contain over 40% of the overall charge of tubulin. They are also hotspots for PTMs that are broadly important for cellular processes including intracellular trafficking, cell division, ciliary beating, neuronal pathfinding, and cardiomyocyte function (Janke & Magiera, 2020; Roll-Mecak, 2020). In addition, the CTTs regulate binding and activity of MAPs, motor proteins, and severing proteins (Fan & McKenney, 2023; Lindsay et al., 2023; McKenney et al., 2016; Niederstrasser et al., 2002; Serrano, Avila, et al., 1984; Serrano et al., 1985; Wang & Sheetz, 2000; Zehr et al., 2020). Despite their importance for microtubule biochemistry and function, little is known about the structure or positioning of the CTTs of α- and β-tubulin. Indeed, the CTTs are assumed to freely extend from the microtubule surface.

Interestingly, molecular modeling approaches suggest that the CTTs undergo interactions with the body of tubulin within the lattice (Freedman et al., 2011; Laurin et al., 2017; Luchko et al., 2008; Sahoo & Hanson, 2025) and thus may not always be exposed along the microtubule surface. To examine the accessibility of the αCTT along the microtubule lattice, we developed a set of three structurally-unrelated biosensors that recognize the native (unmodified) CTT sequence of α-tubulin isotypes that contain a C-terminal tyrosine residue (tyrosinated or Y-αCTT) (**Figure 1C**). The first probe is a fragment antigen binding (Fab) of the rat monoclonal antibody YL1/2 (Kilmartin et al., 1982; Wehland et al., 1983). The second probe is A1aY1, a synthetic protein isolated using yeast display to identify proteins that recognize the CTT sequence of the α-tubulin isotype TubA1A (Kesarwani et al., 2020). The third probe contains the first two CAP-Gly domains of the cytoplasmic linker protein CLIP-170 and was designed based on the known ability of CAP-Gly domains to bind to the Y-αCTT (Bieling et al., 2008; Honnappa et al., 2006; Mishima et al., 2007; Peris et al., 2006; Weisbrich et al., 2007). Notably, the three probes are derived from different protein sources, lending rigor and robustness to our results.

Strikingly, we find that the Y-αCTT probes show limited binding to microtubules when imaged in live cells, suggesting that the α-tubulin CTT is minimally accessible along most microtubules in cells. We find that binding of the Y-αCTT probes to microtubules is increased upon fixation, taxol treatment, or binding of MAPs that induce an expanded lattice state. We also find that microtubule binding of the Y-αCTT probes is enhanced by GTP-locked tubulins in cells but not *in vitro*. Molecular dynamics simulations suggest that the Y-αCTT undergoes more interactions with the tubulin body when tubulin is in the compacted state. These findings suggest that accessibility of the αCTT can be locally regulated by changes to the tubulin conformational state.

RESULTS

Biosensors of αCTT accessibility in the microtubule lattice

We first tested whether the rat monoclonal antibody YL1/2 (Kilmartin et al., 1982; Wehland et al., 1983) could serve as a sensor of Y-αCTT availability. We determined the amino acid sequence of the immunoglobulin G (IgG) heavy and light chains of YL1/2 (**Figure 1D, Figure 1 – Figure Supplement 1A**) and then purified an EGFP-tagged recombinant monoclonal antibody (rMAb) version of YL1/2 (rMAb-YL1/2-EGFP, **Figure 1D, Figure 1 – Figure Supplement 1B**). To confirm that the experimentally-determined protein sequences generate recombinant protein with efficacy and specificity identical to the original antibody, we tested the ability of rMAb-YL1/2-EGFP to recognize the proper antigen using western blotting. We purified glutathione-S-transferase (GST) proteins fused with different human TubA1A αCTT sequences, either full-length [tyrosinated (Y): SVEGEGEEEGEEY], lacking the C-terminal tyrosine [detyrosinated (ΔY): SVEGEGEEEGEE] or lacking the terminal two amino acids (Δ2: SVEGEGEEEGE). The rMAb-YL1/2-EGFP protein recognized the GST-Y sequence by western blot, but not the GST-ΔY or GST-ΔC2 sequences, identical to the commercial YL1/2 antibody (**Figure 1E**). To avoid potential issues with bivalency, we then generated a monovalent EGFP-tagged Fragment antibody binding (Fab) version (**Figure 1D**) by papain digestion and confirmed that the YL1/2^{Fab-}EGFP protein retains the ability to specifically recognize the GST-Y sequence by western blotting (**Figure 1E**).

We next tested A1aY1, a synthetic protein isolated using yeast display to identify proteins that recognize the TubA1A CTT (Kesarwani et al., 2020). We used an A1aY1 probe tagged with superTagRFP (sTagRFP) (**Figure 1F**) as a similar construct with TagRFP-T was previously shown to provide strong recognition of the Y-αCTT (Kesarwani et al., 2020). We were unable to generate recombinant sTagRFP-A1aY1 probe as the protein was prone to aggregation, perhaps due to the oligomeric nature of the sTagRFP moiety (Mo et al., 2020). We thus tested A1aY1 by transient expression in COS-7 cells whose flat morphology enhances visualization of microtubules. We found that sTagRFP-A1aY1 shows little to no microtubule binding in cells that are imaged live (**Figure 1 – Figure Supplement 2A**) but localizes more strongly along microtubules in fixed cells (**Figure 1 – Figure Supplement 2B,C**). We also found that probe localization was sensitive to expression levels as the sTagRFP-A1aY1 probe was diffusely localized at low levels of expression but could decorate the microtubule lattice at higher levels of expression (not shown). To minimize variability in expression levels, we generated a HeLa-Kyoto stable cell line that expresses sTagRFP-A1aY1 in a doxycycline-inducible manner.

We then tested whether a CAP-Gly domain could act as a sensor of Y-αCTT accessibility based on the known ability of CAP-Gly domains to bind to the Y-αCTT (Bieling et al., 2008; Honnappa et al., 2006; Mishima et al., 2007; Peris et al., 2006; Weisbrich et al., 2007). We generated a construct containing the two tandem CAP-Gly domains and part of the first coiled-coil segment of rat CLIP170 (amino acids 3-484) tagged with mScarlet3 (mSc3) (**Figure 1G**) based on a previous “head” domain fragment called H2 (Arnal et al., 2004; Bieling et al., 2008; Scheel et al., 1999). The presence of the coiled-coil segment results in a dimeric protein that contains four CAP-Gly domains (hereafter referred to as 4xCAPGly). We purified recombinant 4xCAPGly-mEGFP protein from *E. coli* (**Figure 1 – Figure Supplement 1B**) and used a far-western blot to verify its specificity for the tyrosinated αCTT sequence of the GST-Y

181 construct (**Figure 1 – Figure Supplement 1C**). When transiently expressed in COS-7 cells and
182 imaged live, 4xCAPGly-mSc3 localized to microtubule plus ends (**Figure 1 – Figure**
183 **Supplement 3A**) due to the presence of a SxIP motif which binds to end binding (EB) proteins
184 located at the growing microtubule plus ends (Bieling et al., 2008). Like A1aY1, fixation caused
185 4xCAPGly-mSc3 to localize along microtubules (**Figure 1 – Figure Supplement 3B,C**). We
186 found that 4xCAPGly-mSc3 localization was also sensitive to expression levels as the probe
187 was diffusely localized at low levels of expression but could decorate the microtubule lattice at
188 higher levels of expression (not shown). To minimize variability in expression levels, we
189 generated HeLa-Kyoto stable cell lines that expresses 4xCAPGly tagged with either mSc3 or
190 mEGFP in a doxycycline-inducible manner.
191 Finally, we tested the specificity of the Y-αCTT probes in reconstitution assays. For
192 these experiments, we purified tubulin from HeLa S3 cells which are largely devoid of tubulin
193 PTMs including detyrosination of the αCTT (Souphron et al., 2019; Thomas et al., 2025). We
194 assembled microtubules from HeLa tubulin and used Taxol to stabilize them in a flow chamber.
195 The Taxol-MTs were either untreated to maintain the tyrosinated state (Y-MTs) or were treated
196 with VASH1/SVBP to generate detyrosinated microtubules (ΔY-MTs) (Thomas et al., 2025).
197 Both the YL1/2^{Fab}-EGFP and 4xCAPGly-mSc3 probes showed stronger decoration of Y-MTs
198 than ΔY-MTs (**Figure 1 H,I**). Taken together, these results demonstrate that we have identified
199 three different probes that specifically recognize the native and unmodified (tyrosinated) α-
200 tubulin CTT.
201
202 ***The αCTT is minimally accessible within a GDP microtubule lattice.***
203 Our initial finding that localization of the A1aY1 and 4xCAPGly probes shifts from
204 cytosolic (A1aY1) or microtubule plus end (4xCAPGly) to the microtubule lattice upon fixation
205 (**Figure 1 – Figure Supplements 2 and 3**) suggests that lattice state impacts the accessibility
206 of the Y-αCTT. Previous work showed that localization of A1aY1 shifts from cytosolic or plus
207 ends to the microtubule lattice in cultured cells treated with SiR-Tubulin (Kesarwani et al., 2020),
208 As SiR-tubulin is a Taxol derivative, it may also convert GDP-tubulin into a GTP-like expanded
209 state (Siahaan et al., 2022). We thus hypothesized that lattice expansion increases the
210 accessibility of the Y-αCTT along at GDP microtubule lattice.
211 To test this idea, we used live-cell imaging to examine the localization of the Y-αCTT
212 probes before and after Taxol treatment. Given the requirements of live-cell imaging and low
213 probe expression, we utilized the stable HeLa-Kyoto cell lines to inducibly express low levels of
214 the probes sTagRFP-A1aY1 (A1aY1 hereafter for brevity) or 4xCAPGly-mEGFP (4xCAPGly
215 hereafter for brevity). In untreated cells, the A1aY1 probe localized diffusely throughout the cell
216 with faint staining along the microtubule lattice observed in some cells (**Figure 2A, before**). No
217 change was observed upon addition of DMSO vehicle control (**Figure 2A,B**). Strikingly, within
218 minutes of Taxol addition, localization of the A1aY1 probe to the microtubule lattice increased
219 1.6-fold (**Figure 2A,C,D**), suggesting that the Y-αCTT is more accessible to the probe after
220 Taxol-induced expansion of the microtubule lattice. To verify these results in another cell line,
221 we transiently expressed the A1aY1 probe in HeLa and COS-7 cells and found a similar
222 increase in microtubule lattice decoration after Taxol treatment (**Figure 2 – Figure Supplement**
223 **1A**).

We carried out similar experiments to examine the response of the 4xCAPGly probe to Taxol treatment. In untreated cells, the 4xCAPGly probe localized to the growing plus ends of microtubules via its association with endogenous EB proteins (**Figure 2E, before**), consistent with previous work (Bieling et al., 2008). No change was observed upon addition of DMSO vehicle control (**Figure 2E,F**). However, within minutes of Taxol treatment, the 4xCAPGly probe relocalized from the ends to the lattice of the microtubules (**Figure 2E,G**), resulting in a 1.5-fold increase in 4xCAPGly probe intensity along the lattice (**Figure 2H**). Relocalization to the microtubule lattice was specific to 4xCAPGly as EB3 protein was lost from the microtubule ends and did not accumulate along the microtubule lattice upon Taxol treatment (**Figure 2 – Figure Supplement 1C).** These results suggest that Taxol-mediated expansion of the microtubule lattice renders the Y-αCTT accessible for 4xCAPGly probe binding. Similar results were obtained when the 4xCAPGly probe was transiently expressed in HeLa or COS-7 cells (**Figure 2 – Figure Supplement 1B**).

Taken together, these results suggest that the Y-αCTT is minimally accessible when tubulin in the microtubule lattice is in the GDP and compacted state but is more accessible for probe binding when GDP-tubulin subunits are pharmacologically converted into a GTP-like expanded state.

MAPs that locally expand the lattice result in a local increase in αCTT accessibility and detyrosination.

In cells, GDP-tubulin can be locally converted into a GTP-like expanded state by binding of specific MAPs to the microtubule lattice. We thus tested whether MAP binding can locally change the ability of the Y-αCTT probes to recognize the microtubule lattice. We transfected the stable A1aY1 and 4xCAPGly cell lines with MAPs known to recognize and/or induce an expanded state. We utilized a rigor version of kinesin-1 [KIF5C^{rigor,} (de Jager et al., 2025; Peet et al., 2018; Shima et al., 2018)] as well as CAMSAP2 and CAMSAP3 (Liu & Shima, 2023; Yue et al., 2023). We also included MAP7 as this MAP was recently suggested to induce and/or preserve an expanded lattice state based on its ability to increase lattice binding of the taxane SiR-tubulin upon overexpression in BEAS-2B cells (Shen & Ori-McKenney, 2024). As controls, we expressed the MAPs tau and MAP2 that recognize and/or induce a compacted lattice state (Castle et al., 2020; Siahaan et al., 2022).

Expression of MAPs that expand the microtubule lattice (KIF5C^{rigor}, CAMSAP2, CAMSAP3, or MAP7) resulted in colocalization of the A1aY1 probe with the expanded lattice (**Figure 3A,C**) whereas expression of MAPs that compact the microtubule lattice did not change (tau) or decreased (MAP2) localization of the A1aY1 probe along microtubules as compared to the control conditions (untransfected or mEGFP-tagged human TubA1A expression) (**Figure 3A,C**). Similar results were found with the 4xCAPGly probe: only expression of the expander MAPs KIF5C^{rigor}, CAMSAP3, or MAP7 resulted in a significant increase in 4xCAPGly probe binding along the microtubule lattice (**Figure 3B,D**). These results indicate that in cells, MAPs that expand the lattice expose the α-tubulin CTT whereas MAPs that compact the lattice do not. We suggest that MAP binding drives a local expansion of the underlying microtubule lattice that results in local switching of the αCTT into an accessible state recognized by the Y-αCTT probes (**Figure 3E**).

267 The ability of MAPs to locally regulate Y-αCTT accessibility suggests that they could
268 regulate downstream events such as posttranslational modification of the αCTT. Consistent with
269 this possibility, the expander MAPs CAMSAP2 and CAMSAP3 enable detyrosination (ΔY) of α-
270 tubulin subunits by the enzyme VASH1/SVBP (Yue et al., 2023). To extend these findings, we
271 tested whether the same expander and compactor MAPs that regulate Y-αCTT accessibility
272 (**Figure 3**) cause an increase in ΔY-MTs. Indeed, like CAMSAP2 and CAMPSAP3 (Yue et al.,
273 2023), expression of the expander MAPs KIF5C^{rigor} or MAP7 resulted in significant increase in
274 ΔY-MTs (**Figure 4A,B**) with the increase in ΔY-MTs localized along the MAP-bound
275 microtubules (**Figure 4A,C**). In contrast, expression of the compactor MAPs tau or MAP2 did
276 not cause an increase in ΔY-MTs (**Figure 4 A,B**) even though, in the case of tau,
277 overexpression caused the microtubules to be bundled in the perinuclear region of the cell
278 (**Figure 4A**).
279
280 ***Nucleotide state regulates αCTT accessibility and detyrosination.***
281 We next tested whether the GTP- vs GDP-state of tubulin can regulate accessibility of
282 the αCTT. To test this in the stable A1aY1 and 4xCAPGly cell lines, we generated a plasmid
283 that expresses PA-tagged human TubA1A with an internal ribosome entry site (IRES) driving
284 the expression of an EGFP reporter protein. We compared WT TubA1A to the mutant E254A
285 which prevents GTP hydrolysis by β-tubulin and therefore locks tubulin in a GTP-bound state
286 (Beckett & Voth, 2023; LaFrance et al., 2022; Roostalu et al., 2020).
287 We transfected the stable A1aY1 and 4xCAPGly cell lines with plasmids for expressing
288 TubA1A(WT) or TubA1A(E254A) and examined the localization of the Y-αCTT probes by live-
289 cell microscopy. Western blotting showed that the tubulin proteins were expressed at
290 comparable levels (**Figure 5 - Figure Supplement 1).** In cells expressing WT TubA1A
291 (visualized by expression of the EGFP reporter), the A1aY1 probe localized in a diffuse manner
292 whereas in cells expressing TubA1A(E254A), the A1aY1 probe localized along the microtubule
293 lattice (**Figure 5A**). Similar results were found for the 4xCAPGly probe which localized to
294 microtubule plus ends in cells expressing TubA1A(WT) but localized along the lattice in cells
295 expressing TubA1A(E254A) (**Figure 5C**). Quantification of these results confirmed that
296 expression of GTP-locked E254A α-tubulin resulted in a significant increase in the density of
297 both A1aY1 and 4xCAP-Gly probes along the microtubule lattice (**Figure 5B,D**).
298 We also examined whether GTP-locked tubulin could cause an increase in
299 detyrosination of the exposed Y-αCTT. We found that expression of GTP-locked E254A α-
300 tubulin but not WT α-tubulin resulted in an increase in ΔY-tubulin levels (**Figure 5E,F**). These
301 results suggest that the nucleotide state of tubulin regulates Y-αCTT accessibility for probe
302 binding and PTM enzymes.
303
304 ***MAPs but not nucleotide state regulate αCTT accessibility in vitro.***
305 We then used reconstitution experiments to directly probe the link between nucleotide
306 state and accessibility of the αCTT. We polymerized HeLa S3 tubulin in the presence of the
307 GTP analog guanosine-5′-[(α,β)-methyleno]tri-phosphate (GMPCPP) to generate microtubules
308 in the GTP-like expanded state (GMPCPP-MTs) or in the presence of GTP which is hydrolyzed
309 to generate the GDP compacted state (GDP-MTs). Furthermore, to directly compare Y-αCTT

310 probe binding between GMPCPP-MTs and GDP-MTs in the same flow chamber, we labeled
311 GMPCPP-MTs with fluorescent Alexa Fluor 568-labeled tubulin and GDP-MTs with fluorescent
312 Alexa Fluor 647-labeled tubulin. We mixed the two microtubule populations with purified Y-αCTT
313 probe proteins (**Figure 1 - Figure Supplement 1B**) in the same chamber and stabilized the
314 microtubules against depolymerization with 25% glycerol. We found that the purified 4xCAPGly
315 probe bound to both microtubule populations (**Figure 6A**) with no significant difference in
316 steady-state binding (**Figure 6B**). Similar results were obtained for the YL1/2^{Fab} protein which
317 bound to both GMPCPP- and GDP-MTs in the flow chamber (**Figure 6C**) with no significant
318 difference in steady-state binding (**Figure 6D**). Thus, although nucleotide state can directly
319 influence tubulin conformational state in cryoEM structures of *in vitro* polymerized microtubules
320 (Alushin et al., 2014; LaFrance et al., 2022; Manka & Moores, 2018; Zhang et al., 2018), it does
321 not appear to directly regulate accessibility of the α-tubulin CTT within the microtubule lattice.
322 The inability of the *in vitro* polymerized microtubules (**Figure 6A-D**) to recapitulate the
323 influence of nucleotide state on αCTT accessibility in cells (**Figure 5A-D**) suggests that the *in*
324 *vitro* assays are missing key factors that regulate αCTT accessibility. We hypothesized that
325 MAPs that recognize the nucleotide and/or conformational state of the microtubule lattice are
326 key to regulating αCTT accessibility. To test this hypothesis in the reconstitution assay, we
327 tested whether the kinesin-1 motor KIF5C could regulate Y-αCTT probe binding. For this, we
328 combined GDP-MTs in a flow chamber with purified KIF5C(1-560) protein and the YL1/2^{Fab}
329 probe protein (**Figure 6E, left arrow**). The ability of KIF5C(1-560) to interact with microtubules
330 and modulate the lattice state can be regulated by nucleotide. In ADP, KIF5C(1-560) binds
331 weakly to microtubules whereas in the absence of nucleotide (apo state), it is locked in a strong
332 MT-bound state that can induce tubulin expansion. In the presence of ATP, KIF5C(1-560) steps
333 along the lattice and induces transient changes in tubulin conformation (Peet et al., 2018; Shima
334 et al., 2018).
335 When KIF5C(1-560) was added in the presence of ADP, the binding of YL1/2^{Fab} to GDP-
336 MTs was reduced as compared to the control condition (no KIF5C) (**Figure 6F,G**). Binding of
337 the YL1/2^{Fab} was even further reduced when KIF5C(1-560) was strongly bound to the GDP-MTs
338 in the apo (no nucleotide) state (**Figure 6F,G**). In contrast, stepping of KIF5C(1-560) in the
339 presence of ATP resulted in a significant increase in YL1/2^{Fab} binding (**Figure 6F,G**).
340 We considered the possibility that Y-αCTT probe binding may be affected by KIF5C
341 binding to the microtubule, *e.g.*, through steric hindrance. We thus separated KIF5C(1-560)
342 microtubule binding from YL1/2^{Fab} microtubule binding using a wash step (**Figure 6E, right**
343 **arrows, Figure 6 – Figure Supplement 1**). After washing out weakly-bound KIF5C(1-560)
344 which does not expand the lattice (ADP condition), YL1/2^{Fab} binding to GDP-MTs was similar to
345 that of the control (no KIF5C) (**Figure 6F,G**). After washing out strongly-bound KIF5C(1-560)
346 (apo state) which does expand the lattice, YL1/2^{Fab} binding to GDP-MTs was significantly
347 increased compared to the control (no KIF5C) or weakly-bound KIF5C(1-560) (ADP state)
348 (**Figure 6F,G**). These results suggest that strong binding of KIF5C(1-560) to the microtubule
349 lattice, either statically in the apo state or transiently in the ATP state, results in increased Y-
350 αCTT probe binding.
351
352 ***Molecular dynamics simulations show numerous transient interactions of the αCTT with***
353 ***the GDP microtubule lattice***

To probe the accessibility of the αCTT at an atomistic level, we performed molecular dynamics (MD) simulations of microtubules in the GDP state. The simulations identified four distinct sites where the acidic residues of the αCTT form salt bridges with basic residues in the tubulin body (**Figure 7A**, **Figure 7 – Figure Supplement 1**). Two of these sites are on the body of the β-tubulin of the adjacent tubulin along the same protofilament (towards the minus end of the microtubule) [**Figure 7A, site 1 (green) and site 2 (cyan**)] whereas the other two sites are on the body of the α-tubulin containing that CTT [**Figure 7A, site 3 (purple) and site 4 (salmon**)]. Since there are seven glutamates in the αCTT and five basic residues each in binding sites 2, 3 and 4, there is a very large multiplicity of interacting conformations between the αCTT and the microtubule (**Video 1**).

We next performed MD simulations of microtubules in the GTP state and found that the αCTT formed electrostatic interactions with the same four binding sites in the tubulin body (**Figure 7A**). In both GDP and GTP microtubules, interactions between the αCTT and the tubulin body occurred most frequently between the N-terminal part of the αCTT (E441 and E443) and site 1 of the adjacent β-tubulin (**Figure 7B**) whereas fewer interactions were observed between the more C-terminal residues of the αCTT (residues E445-E450) and the four binding sites (**Figure 7B**). However, the interactions of the more C-terminal part of the αCTT were more susceptible to the nucleotide state of the lattice. In particular, interactions between residues E445-E450 of the αCTT and site 2 of the adjacent β-tubulin were readily observed in the GDP microtubule but nearly abolished in the GTP microtubule (**Figure 7B**). Likewise, interactions between residues E449 and E450 of the αCTT with site 4 of the α-tubulin body were observed in the GDP microtubules but not the GTP microtubules (**Figure 7B**).

We hypothesized that the decreased interactions between the αCTT and the tubulin body in the GTP microtubule would render the αCTT more accessible when tubulin is in the GTP and expanded state. To test this, we calculated how many C-terminal residues of the tail (E445 to Y451) were inaccessible (*i.e.* bound to one of the tubulin body sites) throughout the course of the simulations. We found that the αCTT residues in the GDP microtubule showed increasing interactions with the tubulin body as a function of time and reached more than 40% inaccessibility after about 300 ns (**Figure 7C**). In contrast, the αCTTs in the GTP microtubule were only about 10% inaccessible throughout the entire simulation time (**Figure 7C**). Taken together, these results support the hypothesis that the αCTT undergoes frequent interactions with the GDP-containing microtubule lattice that render it largely inaccessible to the Y-αCTT probes.

DISCUSSION

The αCTT is more accessible along expanded microtubules

In this work, we sought to gain an understanding of the relative accessibility of the αCTT along the microtubule. To this end, we developed three probes to visualize the tyrosinated αCTT: YL1/2^{Fab}, A1aY1, and 4xCAPGly. We note that our probes are not expected to recognize the two α-tubulin isotypes that do not have a genetically encoded C-terminal tyrosine, TubA4A and TubA8, and play roles in brain development and spermatogenesis, respectively (Benkirane et al., 2024; Diggle et al., 2017; Hausrat et al., 2021). The YL1/2^{Fab} and 4xCAPGly proteins can be purified for reconstitution assays whereas the A1aY1 and 4xCAPGly probes can be expressed in cells although their optimal use requires live-cell imaging. It is possible that fixation causes the microtubule lattice to expand, but we cannot exclude alternative explanations, *e.g.*, that fixation disrupts CTT-binding sites on the tubulin body. We also found that high levels of Y-αCTT probe expression can drive their binding to the microtubule lattice, and it is thus critical to limit examination to cells that express low levels of our probes. This is an important caveat to keep in mind in experiments that utilize transient transfection of these Y-αCTT probes.

We found that the A1aY1 and 4xCAPGly probes showed minimal binding to the microtubule lattice in cells under normal culture conditions. This finding suggests that the αCTT is generally not accessible along the microtubule lattice. Faint microtubule localization is more commonly observed with A1aY1 when compared to 4xCAPGly, which may be due to higher affinity interactions of 4xCAPGly with EB1 and other proteins at the microtubule plus end versus the microtubule lattice. The weak lattice binding of the αCTT probes was surprising as the tubulin CTTs are thought to freely protrude from the microtubule lattice.

Expansion of the microtubule lattice via three orthogonal approaches resulted in an increase in Y-αCTT probe binding: 1) treatment of cells with Taxol (**Figure 2**), 2) expression of MAPs that expand tubulin within the microtubule lattice (expander MAPs) (**Figure 3**), and 3) expression of a GTP-locked α-tubulin mutant (E254A, **Figure 5**). These results suggest that accessibility of the αCTT is regulated by the compacted versus expanded state of tubulins within the microtubule lattice. We note that “expanded” and “compacted” are used as terms relative to one another rather than defined against a standard microtubule structure (LaFrance et al., 2022).

The simplest mechanistic explanation for how tubulin conformational state regulates αCTT accessibility is that the nucleotide state gates αCTT accessibility. However, we find that YL1/2^{Fab} and 4xCAPGly probes bind similarly to GMPCPP-MTs vs GDP-MTs polymerized *in vitro* (**Figure 5**). At first glance, these data conflict with our observation that VASH1/SVBP preferentially detyrosinates microtubules that are in an expanded state (Yue et al., 2023). However, it is possible that an expanded lattice promotes activation of VASH1/SVBP, or, alternatively, that engagement of the αCTT with the catalytic site of VASH1/SVBP is optimal on expanded microtubules. Future work is necessary to address these interesting possibilities.

There are several explanations for why αCTT accessibility in reconstitution assays (**Figure 6A-D**) does not correlate with the structural state of the microtubule lattice as observed in cells (**Figure 5**). First, microtubule assembly *in vitro* may not produce a lattice state resembling that in cells, either due to differences in protofilament number and/or buffer

conditions and/or the lack of MAPs during polymerization. Second, the αCTT may switch between accessible and inaccessible states in both GDP- and GTP-microtubules, but the conformation switch rate differs between GDP-microtubules vs GTP-microtubules. In this scenario, Y-αCTT probes would be expected to saturate αCTT-binding sites on both GDP- and GTP-microtubules *in vitro*. Consistent with this possibility, our MD simulations show that the αCTT undergoes transient interactions with multiple sites along the microtubule lattice. Third, MAPs that bind to or induce an expanded lattice may promote Y-αCTT accessibility. Indeed, we demonstrate that the addition of expander MAPs can increase Y-αCTT accessibility both in cells (**Figure 3**) and for microtubules polymerized under *in vitro* conditions (**Figure 6E-G**).

The αCTT is sequestered through interactions with the tubulin body

We propose that the αCTT is sequestered along the microtubule through interactions with the tubulin body in a manner that precludes its recognition by the Y-αCTT probes. Indeed, our MD simulations show that the αCTT undergoes frequent interactions with the bodies of α-tubulin (*cis* interactions) and β-tubulin (*trans* interactions). These findings are consistent with an NMR study showing that the αCTT can interact with the body of the α,β-tubulin dimer (Wall et al., 2016) and with recent molecular modeling studies suggesting that the CTTs form frequent contacts with themselves and the microtubule body (Freedman et al., 2011; Laurin et al., 2017; Luchko et al., 2008). Furthermore, our data are in agreement with recent modeling work suggesting that CTT-lattice interactions are primarily observed for the αCTT interacting with the *β*-tubulin of the neighboring dimer towards the minus direction along a single protofilament (Sahoo & Hanson, 2025). Our work extends these findings by identifying four primary sites of αCTT-tubulin interactions.

Site 1 involves interactions of the N-terminal glutamate residues of the αCTT (E441, E443) with adjacent β-tubulin basic residues (R390, R391, K392) and our simulations indicate that these interactions are similar between GDP and GTP microtubules. Interestingly, this contact site has been previously observed by cryo-electron microscopy. Specifically, Bodey et al. determined a 9 Å structure of Taxol-stabilized bovine brain microtubules decorated with the kinesin-5 motor domain and observed density corresponding to the αCTT interacting with β-tubulin of the neighboring tubulin along the longitudinal axis (Bodey et al., 2009). More recently, Zehr and Roll-Mecak determined a 2.9 Å structure of GMPCPP-stabilized microtubules polymerized from α1B/βI + α1/βIVb tubulins and observed contacts between V437, S439, and E441 of α-tubulin and residues R390 and R391 of the longitudinally adjacent β-tubulin (Zehr & Roll-Mecak, 2023).

In contrast, the interactions at sites 2, 3, and 4 have not been observed in previous modeling or structural studies. These interactions involve salt bridges between acidic residues at the C-terminal end of the αCTT (E445-E450) and clusters of basic residues on the adjacent β-tubulin (site 2: K174, R380, R213, K379, and R306) or on the α-tubulin itself (site 3: K311,R308, K338, R339 and site 4: K112,R123, R156, K163, K430). We note that these interactions are energetically favorable since the salt bridges are a strong enthalpic interaction and the multitude of conformations reduces the entropic penalty. The multiplicity of interactions between the αCTT and the microtubule lattice explains why such interactions are not able to be resolved in structural studies. Moreover, the transient nature of these interactions explains why

475 the Y-αCTT probes show no difference in steady-state binding between reconstituted GMPCPP
476 and GDP microtubules. Importantly, our simulations indicate that the *trans* interactions with site
477 2 and the *cis* interactions with site 4 are reduced in the GTP state, consistent with the αCTT
478 being more accessible along a GTP expanded microtubule lattice.
479
480 ***Crosstalk between CTTs, MAPs, and PTMs***
481 Overall, our data support a model in which the αCTT is generally not accessible along
482 the GDP-microtubule but can be locally "exposed" by MAPs. We speculate that, in cells, the
483 microtubule lattice is decorated by MAPs that preferentially recognize the compacted GDP-
484 lattice state and that these compactor MAPs in turn mask the αCTT and/or stabilize αCTT
485 interactions with the microtubule lattice. Lattice expansion, ***e.g.***, through Taxol treatment or
486 overexpression of expander MAPs, would evict compactor MAPs and result in exposure of the
487 αCTTs. Identification of compactor MAPs that help to conceal the αCTT is a major area for
488 future work and represents a significant challenge because our current knowledge of MAPs that
489 bind MTs in a conformation-sensitive manner is limited. Moreover, compactor MAPs may
490 function synergistically or in concert, complicating the identification of MAPs that regulate αCTT
491 accessibility.
492 An important implication of our work is that the αCTT is not freely available to undergo
493 posttranslational modification. Indeed, we find a strong correlation between the perturbations we
494 used to expand the microtubule lattice and the presence of ΔY-MTs. Taxol treatment expands
495 the microtubule lattice and promotes detyrosination (Yue et al., 2023) as does expression of
496 expander MAPs but not compactor MAPs (**Figure 3**) or expression of a GTP-locked tubulin
497 (**Figure 4**). Our findings may also apply to other PTMs of the αCTT, *i.e.*, polyglycylation and
498 polyglutamylation. This possibility is supported by observations showing that polyglutamylation
499 and detyrosination often co-localize in cells (Ebberink et al., 2023) although further pursuit of
500 this possibility is complicated by the fact that the CTTs of both α- and β-tubulin can be modified
501 with glutamylation and we generally lack tools to distinguish between α-tubulin and β-tubulin
502 glutamylation. In addition, it is not known if the accessibility of the βCTT is regulated in a
503 manner similar to the αCTT. Recent findings showing that MATCAP2/TCMP2 trims the CTT of
504 β1-tubulin to generate Δ3-β1 and that this modified β1-tubulin localizes to specific subcellular
505 structures strongly suggest that post-translational modification of the βCTT is also regulated
506 (Nicot et al., 2023). Our work provides a conceptual roadmap to explore this interesting
507 possibility.
508 A second important implication of our work is how the αCTT can spatially and temporally
509 influence the binding of MAPs to the microtubule. For example, the molecular motors dynein
510 and kinesin-3 KIF13B contain CAP-Gly domains and their initial microtubule interactions (on-
511 rates) are thus facilitated by a tyrosinated αCTT (Fan & McKenney, 2023; McKenney et al.,
512 2016; Niederstrasser et al., 2002). We speculate that these motor proteins preferentially target
513 microtubule segments where expander MAPs have exposed the αCTT. In addition, kinesin-1
514 expands the microtubule lattice (Peet et al., 2018; Shima et al., 2018) and as MAP7 is now also
515 thought to expand the lattice [Figures 3,4 (Shen & Ori-McKenney, 2024)], we speculate that the
516 ability of MAP7 to facilitate the loading of kinesin-1 onto microtubules may involve lattice
517 expansion in addition to protein-protein interactions between MAP7 and kinesin-1 (Chaudhary et

518 al., 2019; Ferro et al., 2022; Hooikaas et al., 2019; Metivier et al., 2019; Monroy et al., 2020;
519 Pan et al., 2019; Tymanskyj et al., 2018). Further work will address these and other outstanding
520 questions about the interplay between microtubule lattice state, MAPs, and molecular motors.
521

522 **MATERIAL AND METHODS**
523
524 **Y-αCTT probe plasmids**
525 The 4xCAPGly probe consists of rat CLIP1 (CLIP-170) aa 3-484 and is based on a fragment
526 of CLIP-170 previously called H2 (Arnal et al., 2004; Bieling et al., 2008; Scheel et al., 1999). To
527 generate a plasmid for transient mammalian expression of a C-terminally tagged 4xCAPGly probe,
528 the DNA coding for amino acids 3-484 of rat CLIP1 (Uniprot Q9JK25) was prepared by PCR
529 amplification using the primers CAPGLYfor1 and CAPGLYrev1 (Supplementary File 1). The PCR
530 fragment was joined with BamHI-linearized pmEGFP-N1 or pmScarlet3-N1 [mSc3, (Gadella et al.,
531 2023)] vectors via Gibson Assembly (NEB) to create pN1-4xCAPGly-mEGFP and pN1-4xCAPGly-
532 mSc3 plasmids.
533 To generate a stable knock-in HeLa-Kyoto cell line expressing 4xCAPGly, the DNA for
534 4xCAPGly-mEGFP and 4xCAPGly-mS3 were amplified by PCR using primers CAPGLY_for2 and
535 CAPGLY_revGFP or CAPGLY_revSc3 (Supplementary File 1). The PCR fragments were inserted
536 via Gibson Assembly (NEB) into a pEM791 vector that was digested with AgeI and BsrGI. The
537 pEM791-4xCAPGly-mEGFP and pEM791-4xCAPGly-mS3 plasmids were used to establish knock-in
538 HeLa cell lines via recombination mediated cassette exchange (Khandelia et al., 2011) in order to
539 express 4xCAPGly-mEGFP or 4xCAPGly-mS3 proteins in a doxycycline-inducible manner.
540 To generate a plasmid for bacterial expression of a 6×His-tagged 4xCAPGly-mEGFP probe,
541 the DNA coding for 4×CAPGly-mEGFP was PCR amplified from the pmEGFP-N1-4xCAPGly
542 plasmid using primers CLIP_for3 and CLIP_rev3 (Supplementary File 1). The PCR fragment was
543 joined with a BamHI-linearized pET15b vector via Gibson Assembly (NEB).
544 To generate a plasmid for transient mammalian expression of the superTagRFP-tagged A1aY1
545 probe, a 232 bp fragment of A1aY1 lacking the start codon was synthesized (IDT) and PCR
546 amplified using the primers A1aY1_for1 and A1aY1_rev1 (Supplementary File 1). The PCR fragment
547 was inserted into a EcoRI-linearized psuperTagRFP-C1, in which mEGFP of pmEGFP-C1 vector
548 had been replaced with superTagRFP [sTagRFP, (Mo et al., 2020)] using Gibson Assembly,
549 resulting in the plasmid pC1-superTagRFP-A1aY1.
550 To generate a stable knock-in HeLa-Kyoto cell line expressing superTagRFP-A1aY1, the
551 coding sequence was amplified from pC1-superTagRFP-A1aY1 using the primers A1aY1_for2 and
552 A1aY1_rev2 (Supplementary File 1) and inserted into a pEM791 vector that was linearized by
553 digestion with AgeI and BsrGI. The resulting pEM791-superTagRFP-A1aY1 plasmid was used to
554 establish a knock-in HeLa cell line via recombination mediated cassette exchange (Khandelia et al.,
555 2011) in order to express superTagRFP-A1aY1 protein in a doxycycline-inducible manner.
556 To generate a plasmid for bacterial expression of the A1A1 probe, we placed the fluorophore
557 at the C-terminus of A1aY1 based on a previously published study (Kesarwani et al. 2020).
558 Fragments of superTagRFP and A1aY1 were separately PCR-amplified with primers A1aY1_for3
559 and A1aY1_rev3, and sTagRFP_for1 and sTagRFP_rev1 (Supplementary File 1), respectively.
560 These two fragments were inserted then into BamHI-linearized pET15b vector via Gibson Assembly,
561 which yielded the construct pET15b-6xHis-A1aY1-superTagRFP. This construct was used to
562 produce the recombinant fusion protein 6xHis-A1aY1-sTagRFP.
563
564 **Tubulin plasmids**
565 The plasmid for expressing PA-tagged human TubA1A WT and E254A constructs was
566 generated by replacing the 6xHis tag inserted between Ile42 and Gly43 in the flexible loop of
567 TubA1A in the vectors pJM546 and pJM602 (kindly provided by Jeff Moore, University of Colorado
568 Anschutz Medical Center) with a PA-tag (GVAMPGAEDDVV). The resulting plasmids contain PA-
569 tagged TubA1A followed by an internal ribosome entry site (IRES) driving the expression of an
570 EGFP reporter. The template plasmids were PCR amplified using phosphorylated primers His-
571 PA_for and His-PA_rev (Supplementary File 1), and ligated, yielding pCAGGS-internal PA-TubA1A-
572 IRES-EGFP. For immunofluorescence studies, constructs without the IRES-GFP component were
573 used. These versions were generated by amplifying the full vectors excluding the IRES-GFP region

using phosphorylated primers IRES-GFP_removal_for and IRES-mEGFP_removal_rev (Supplementary File 1), followed by ligation to re-circularize the vectors.

For GFP-tagged TubA1A expression, untagged TubA1A was amplified using primers mEGFP-TubA1A_for and mEGFP-TubA1A_rev, and inserted into a pCAGGS vector that had been linearized with primers IRES-GFP_removal_for and pCIG2_rev (Supplementary File 1). The insertion was performed via Gibson assembly, yielding the pCAGGS-mEGFP-TubA WT construct.

MAP plasmids

MAP2 and MAP7 were tagged at their N-termini with the PA tag and at their C-termini with mEGFP (PA-MAP2-mEGFP and PA-MAP7-mEGFP). The coding sequence of human MAP2 (UniProt P11137-4) was amplified from cDNA (Horizon Discovery; Clone ID 5223046) using primers MAP2_for and MAP2_rev (Supplementary File 1). The coding sequence of mouse MAP7 (Uniprot O88735-2) was amplified from pCAGG-MAP7(FL)-mCherry (Tymanskyj et al., 2018) using primers MmMAP7_for and MmMAP7_rev for MAP7 (Supplementary File 1). The PCR products were used as inserts in a Gibson assembly reaction with pPA-mEGFP-N1-EML2-S plasmid (Hotta et al., 2022) that was linearized and PCR-amplified with primers PA-mEGFP-N1_for1 and PA-mEGFP-N1_rev1 (Supplementary File 1).

For the Kif5C^{rigor} construct, the rat Kif5C(1-560,G235A) sequence (Uniprot P56536) was amplified from pN1-KIFC(1-560,G235A) using primers Kif5C_for and Kif5C_rev (Supplementary File 1). The resulting PCR product was used as an insert in a Gibson assembly with the pmEGFP-N1 vector linearized and PCR-amplified with primers PA-mEGFP-N1_for2 and PA-mEGFP-N1_rev2.

Tau, CAMSAP2, and CAMSAP3 were tagged at their N-termini with mEGFP. Human tau (Uniprot P10636-6) was PCR-amplified from cDNA (Horizon Discovery, Clone ID 40007445) using primers tau_for and tau_rev (Supplementary File 1). Human CAMSAP2 (Uniprot Q08AD1-1) was PCR-amplified from pEGFP-C1-CAMSAP2 (Yue et al., 2023) using primers CAMSAP2_for and CAMSAP2_rev (Supplementary File 1). Human CAMSAP3 (Uniprot Q9P1Y5-2 with N-terminal 19 amino acid deletion) was PCR-amplified from cDNA (Horizon Discovery, Clone ID, 3868695) using primers CAMSAP3_for and CAMSAP3_rev (Supplementary File 1). The PCR products were used as inserts in a Gibson assembly reaction with the pPA-mEGFP-C1 vector (Hotta et al., 2022) linearized by EcoRI digestion.

In some cases, transient expression of these MAPs suppressed the expression of Y-αCTT probes in the knock-in HeLa cell lines. To mitigate this, mEGFP-tagged tau, MAP2, CAMSAP2, and CAMSAP3 were further transferred into pCAGGS vectors containing a β-actin promoter. The pCAGGS vector was PCR-amplified with primers pCAGGS_for and pCAGGS_rev (Supplementary File 1) and the inserts were added by Gibson assembly. The primers mEGFP_MAP_for and mEGFP_MAP_rev were used to PCR-amplify inserts of mEGFP-tau, mEGFP-CAMSAP2, and mEGFP-CAMSAP3 whereas the primers mEGFP_MAP_for and PA-MAP2-mEGFP_rev were used to PCR-amplify the insert of MAP2-mEGFP. All plasmids were validated by Sanger sequencing.

Generation of rMAb-YL1/2-EGFP antibody and Fab

We determined the protein sequences of the immunoglobulin G (IgG) heavy and light chains of the rat monoclonal anti-tyrosinated α-tubulin antibody YL1/2 using mass spectrometry (Rapid Novor). As leucine and isoleucine have the same mass, their identities were distinguished by further fragmentation at the Cβ-Cγ bond to release a propyl (leucine) or ethyl (isoleucine) group [W-ion determination, Rapid Novor (Zhokhov et al., 2017)]. The Clothia method was used to identify the three complementarity determining regions (CDRs) within the variable regions of each light chain and heavy chain (Chothia & Lesk, 1987). CDRs are hypervariable loops that form the antigen binding interface and thus determine antibody specificity and affinity. The surrounding sequences (framework regions) dictate and maintain the folded state of the variable domain such that the CDRs are properly displayed on one side of the folded protein (Zhu et al., 2025).

To generate a recombinant monoclonal antibody (rMAb), the coding sequences of the HC and LC were tagged at the N-terminus with a signal sequence (MGWSCIILFLVATATGVHS) for entry into the secretory pathway. The coding sequence of the LC was additionally modified by tagging the

627 C-terminus with a GGGGS linker followed by EGFP. Recombinant YL1/2-EGFP protein was
628 produced using the CHO-Express system (Genscript). A Fab fragment of the YL1/2-EGFP protein
629 was prepared using the Fab Preparation Kit (Thermo Fisher Scientific; Cat# 44985). Briefly,
630 recombinant YL1/2-EGFP protein was digested with papain for 5 hours at 37ºC followed by negative
631 purification via a Protein A column. Flow-through fractions from the Protein A column were combined
632 and concentrated using an Amicon Ultra-10K ultrafiltration device (Millipore, Cat# UFC801024). The
633 YL1/2^{Fab}-EGFP (dissolved in 1×PBS) was aliquoted, flash frozen, and stored at -80ºC until use.
634
635 ***Protein Expression and Purification***
636 The 6×His-tagged 4xCAPGly-mEGFP protein was expressed in BL21-CodonPlus-RILC *E.*
637 *coli* cells. Bacterial cultures were induced with 0.5 mM IPTG at 18°C for 18 hr. Purification was
638 performed based on (Bieling et al., 2008). Cell pellets were resuspended in lysis buffer [50 mM KPi
639 (pH 7.5), 500 mM NaCl, 1 mM $MgCl_2$, 1 mM BME, 1 mM PMSF, 1.0 mg/ml lysozyme, 1 ×
640 SIGMAFAST, and Benzonase nuclease], sonicated, and clarified by centrifugation. The lysate was
641 applied directly to Ni-NTA resin that was pre-equilibrated with lysis buffer. Once the protein was
642 bound, the column was washed with 10 column volumes of low imidazole wash buffer [50 mM KPi
643 (pH 7.5), 500 mM NaCl, 1 mM $MgCl_2$, 8.5 mM Imidazole (pH 7.4), and 1 mM BME] followed by an
644 additional wash with 3 column volumes of high imidazole wash buffer [50 mM KPi (pH 7.5), 500 mM
645 NaCl, 1 mM $MgCl_2$, 125 mM Imidazole (pH 7.4), and 1 mM BME]. Proteins were eluted with elution
646 buffer [50 mM KPi (pH 7.5), 500 mM NaCl, 1 mM $MgCl_2$, 300 mM Imidazole (pH 7.4), and 1 mM
647 BME]. Fractions containing the protein were combined and gel filtered over a HiLoad 16/600
648 Superdex 200 column that was equilibrated with 50 mM KPi (pH 7.5), 150 mM NaCl, 1 mM $MgCl_2$,
649 and 1 mM BME. Fractions containing the protein were pooled, concentrated with an appropriately
650 sized MWCO centrifugal concentrator, aliquoted, flash frozen, and stored at -80°C until use.
651 The 6×His-sTagRFP-A1aY1 protein was expressed in Rosetta 2(DE3) pLysS *E. coli* cells.
652 The 6×His-sTagRFP-A1aY1 protein was purified similarly as the 4xCAPGly proteins with the
653 following changes: the cells were lysed in lysis buffer [50 mM KPi (pH 7.5), 500 mM NaCl, 20 mM
654 imidazole, 1 mM PMSF, 1 × SIGMAFAST, and Benzonase]. The low imidazole wash step was
655 omitted and the column was washed with Ni-NTA wash buffer [50 mM KPi (pH 7.5), 500 mM NaCl,
656 20 mM imidazole, 1 mM MgCl2, 1 mM ATP and SIGMAFAST] and protein was eluted from the
657 column with elution buffer [50 mM KPi (pH 7.5), 500 mM NaCl, 200 mM imidazole]. The protein was
658 separated by gel filtration using buffer [10 mM Hepes, 300 mM KCl, 1 mM DTT (pH 7.5)]. Protein
659 concentration was determined via Bradford protein assay.
660 The KIF5C(1-560) protein was expressed in Sf9 cells. The cells were cultured in suspension
661 with serum-free sf900 II SFM medium supplemented with antibiotic antimycotic in flasks at 28°C in a
662 non-CO_2 nonhumidified incubator with an orbital shaker platform set at 110 rpm. The KIF5C(1-560)
663 protein consists of rat KIF5C aa 1-160 fused to Halo tag and a dual StrepII tag [KIF5C(1-560)-Halo-
664 2xstreptII]. The construct was subcloned into the pFastBac1 vector via Gibson assembly.
665 Baculovirus was generated according to the Bac-to-Bac system (Thermo Fisher). In brief, plasmids
666 were transformed into DH10Bac *E. coli* to generate recombinant bacmids. Bacmid DNA was isolated
667 with the HiPure Plasmid DNA miniprep kit and confirmed by PCR analysis. Recombinant bacmid
668 DNA was transfected into Sf9 cells using Cellfectin II. After 7 d, the supernatant containing P1
669 baculovirus was collected and clarified by centrifugation at 3,000 rpm for 3 min at 4°C. The
670 baculovirus was amplified by successive infection of Sf9 cells to generate P2 and P3 baculoviruses.
671 Baculovirus-containing supernatants were stored at 4°C in the dark. To purify KIF5C(1-560)-Halo-
672 StrepII protein, Sf9 cells were infected with 3% P3 baculovirus (vol/vol). After 3 d, the cells were
673 harvested by centrifugation for 15 min at 3,000 rpm at 4°C. The pellet was washed once with PBS
674 and resuspended in ice-cold lysis buffer (200 mM NaCl, 4 mM $MgCl_2$, 0.5 mM EDTA, 1 mM EGTA,
675 0.5% igepal, 7% sucrose, and 20 mM imidazole-HCl, pH 7.5) supplemented with 2 mM ATP, 1 mM
676 PMSF, 5 mM DTT, and protease inhibitor cocktail. After 30 min incubation on ice, the lysates were
677 clarified by ultracentrifugation for 20 min at 20,000 rpm in F12-8x50y rotor (Sorvall 3421), and the
678 supernatants were incubated with strep-Tactin beads for 1h at 4°C with rotation. The beads were
679 transferred to a PD-10 column and washed with wash buffer (150 mM KCl, 25 mM imidazole-HCl,

680 pH 7.5, 5 mM $MgCl_2$, 1 mM EDTA, and 1 mM EGTA) supplemented with 1 mM PMSF, 3 mM DTT, 3
681 mM ATP, and protease inhibitor cocktail. Bound proteins were eluted in 6x0.5 mL fractions with
682 elution buffer (25 mM KCl, 25 mM imidazole-HCl, pH 7.5, 5 mM EGTA, 2 mM $MgCl_2$, 2 mM DTT, 0.1
683 mM ATP, 1 mM PMSF, protease inhibitor cocktail and 10% glycerol) supplemented with 50 mM
684 biotin. The fractions were separated by SDS-PAGE and fractions containing KIF5C(1-560) were
685 combined and dialyzed in dialysis buffer (25 mM imidazole-HCl, pH 7.5, 25 mM KCl, 5 mM EGTA, 2
686 mM $MgCl_2$, 2 mM DTT, 0.1 mM ATP and 10% glycerol). After 2 hr, the buffer was changed with fresh
687 dialysis buffer and dialyzed overnight at 4°C to remove biotin from the sample. The protein was
688 concentrated by centrifugation, and aliquots were snap frozen in liquid nitrogen and stored in -80°C
689 until further use.
690
691 ***Western Blot Analysis***
692 The specificity of the Y-αCTT probes for the tyrosinated αCTT was validated utilizing GST-
693 αCTT fusion proteins in which glutathione-S-transferase (GST) was fused to human TubA1A αCTT
694 sequences representing tyrosinated (Y = SVEGEGEEEGEEY), detyrosinated (ΔY =
695 SVEGEGEEEGEE), or ΔC2 (Δ2 =SVEGEGEEEGE) tails. GST-αCTT proteins were expressed and
696 purified from bacteria as previously described (Hotta et al., 2022; Hotta et al., 2023). GST-αCTT
697 proteins (250 ng) were separated by SDS-PAGE and transferred on to nitrocellulose membranes.
698 The membranes were blocked with 3% skim milk in 1 × TBS supplemented with 0.1% tween-20
699 (TBST blocking buffer) for 1 hr at room temperature followed by incubation with primary and
700 secondary antibodies (Key Resource Table) for 1 hr at room temperature. Alternatively, membranes
701 were incubated with recombinant proteins rMAb-YL1/2-EGFP (2 mg/mL), $YL1/2^{Fab}$-EGFP (4 mg/mL),
702 or 4×CAPGly-mEGFP protein (100 nM) in blocking buffer for 30 min at room temperature.
703 HeLa cell lysates were prepared by resuspending cell pellets in lysis buffer (6 mM Na_2HPO_4,
704 4 mM NaH_2PO_4, 2 mM EDTA, 150 mM NaCl, 1% NP40 and protease inhibitors) followed by a brief
705 sonication and clarification via centrifugation. Cell lysates (15 μg) were separated by SDS-PAGE
706 and transferred to nitrocellulose membranes. The membranes were blocked with 5% slim milk in
707 PBS supplemented with 0.5% tween-20 (PBST blocking buffer), and primary antibody incubation
708 was carried out at 4ºC overnight. Primary antibodies and dilutions are listed in Key Resources Table.
709 After incubation with primary antibodies, the membranes were washed 3-5 times for 5 min each with
710 the TBST blocking buffer or PBST and then incubated with the corresponding secondary antibodies
711 for 1 hr at room temperature. Secondary antibodies and dilutions are listed in the Key Resources
712 Table. Membranes were washed 3-5 times for 5 minutes each. Fluorescence signals were detected
713 with the Azure 600 imaging system.
714
715 ***Mammalian cell maintenance and transfection***
716 COS-7 cells were grown in Dulbecco's modified Eagle medium (DMEM) supplemented with
717 10% (vol/vol) Fetal Clone III and 2 mM GlutaMAX. HeLa Kyoto cells [female *Homo sapiens*
718 (RRID:CVCL_1922)] were maintained in DMEM containing 10% fetal bovine serum (FBS) and 1%
719 Penicillin-Streptomycin. HeLa Kyoto knock-in cell lines expressing 4xCAPGly-mEGFP, 4xCAPGly-
720 mSc3 and sTagRFP-A1aY1 in a doxycycline-inducible manner were maintained in DMEM containing
721 10% FBS, 1% Penicillin-Streptomycin, and 1 mg/mL puromycin. The expression of each transgene
722 in each knock-in cell line was induced via the addition of 2 μg/mL doxycycline. HeLa S3 cells were
723 grown in suspension in DMEM supplemented with 10% (vol/vol) Fetal Clone III Serum, 2 mM
724 GlutaMAX, and 1% Penicillin/Streptomycin.
725 All cell lines were maintained in the presence of 5% CO_2 at 37ºC. All cell lines were
726 screened and found negative for mycoplasma contamination. HeLa and COS-7 cells were
727 transfected with Lipofectamine 2000 according to the manufacturer's instructions. Briefly, 0.5-1 μg of
728 plasmid DNA was diluted in 250 μL of Opti-MEM. Following a 5 min incubation at room temperature,
729 250 μL of Opti-MEM containing 5 μL of Lipofectamine 2000 was added to the plasmid DNA and
730 incubated for 20 min at room temperature. The entire reaction mixture was added directly to the dish
731 of cells containing 1 mL of Opti-MEM and incubated for 3.5 hours at 37ºC before exchanging the
732 media to DMEM supplemented with 10% FBS and 1% Penicillin-Streptomycin.

733
734 ***Total internal reflection fluorescence microscopy***
735 All assays used HeLa microtubules. For this, tubulin was purified from HeLa S3 cells using a
736 GST-TOG column and polymerized into microtubules as described (Thomas et al., 2025). A flow cell
737 (~10 μl volume) was assembled by attaching a clean #1.5 coverslip (Fisher Scientific) to a glass
738 slide (Fisher Scientific) with two strips of double-sided tape. All imaging was performed at room
739 temperature. *In vitro* assays were performed on an inverted Nikon Ti-E/B total internal reflection
740 fluorescence microscope with a perfect focus system, a 100 × 1.49 NA oil immersion TIRF objective,
741 three 20 mW diode lasers (488 nm, 561 nm, and 640 nm) and EMCCD camera (iXon+ DU879;
742 Andor). Image acquisition was controlled using Nikon Elements software.
743 To validate the sensitivity of the Y-αCTT probes to the tyrosinated vs detyrosinated state of
744 α-tubulin, AlexaFluor 488- or 647-labeled microtubules were generated. Taxol-stabilized
745 microtubules were incubated in a flow chamber with cell lysate overexpressing VASH1 and SVBP for
746 15 minutes to generate ΔY-microtubules (Thomas et al., 2025; Yue et al., 2023). The chambers
747 were washed with 0.1 mg/ml casein and 10 μM Taxol in BRB80 to remove VASH1/SVBP enzyme.
748 Then an imaging mixture containing YL1/2^{Fab}-EGFP (66 nM) or 4xCAPGly-mEGFP (15 nM) proteins
749 in 10 μM Taxol in BRB80 supplemented with 0.1 mg/ml casein and oxygen scavengers (1 mM DTT,
750 1 mM $MgCl_2$, 10 mM glucose, 0.2 mg/ml glucose oxidase, and 0.08 mg/ml catalase) was flowed into
751 the chambers and imaged.
752 To compare Y-αCTT probe binding to GMPCPP vs GDP microtubules, microtubules were
753 polymerized from HeLa S3 tubulin in the presence of GMPCPP or GTP and in the presence of
754 AlexaFluor 568-labeled HeLa tubulin or AlexaFluor 647-labeled HeLa tubulin (Thomas et al., 2025).
755 The chambers were prepared by first flowing in a recombinant anti-TubB3 Tuj1 antibody (gift from
756 Jeffrey Moore, University of Colorado Anschutz Medical Center) diluted 1:50 in BRB80 and
757 incubating for 5-10 min. Chambers were washed with 25% glycerol in BRB80, and then a mixture of
758 GMPCPP and GDP microtubules was added and incubated for 5-10 min. The chambers were
759 washed with 25% glycerol/BRB80 and then YL1/2^{Fab}-EGFP (final concentration of 66 nM) or
760 4xCAPGly-mEGFP (final concentration of 15 nM) proteins were added in 25% glycerol/BRB80
761 supplemented with 0.1 mg/ml casein and oxygen scavengers (1 mM DTT, 1 mM $MgCl_2$, 10 mM
762 glucose, 0.2 mg/ml glucose oxidase, and 0.08 mg/ml catalase).
763 To examine whether the binding behavior of YL1/2^{Fab}-EGFP on glycerol-stabilized GDP-MTs
764 is regulated by KIF5C(1-560)-Halo protein, GDP-MTs were assembled from HeLa S3 tubulin and
765 stabilized in 25% glycerol/BRB80. The microtubules were introduced into a flow cell and incubated
766 for 3 min at room temperature to allow for nonspecific adsorption to the coverslips. After washing
767 with blocking buffer [1 mg/mL casein and 25% glycerol in P12 buffer (12 mM PIPES/KOH pH 6.8, 2
768 mM $MgCl_2$, 1 mM EGTA)], the flow cell was infused with imaging buffer (P12 buffer supplemented
769 with 25% glycerol, 0.3 mg/ml casein, and oxygen scavenger mix) with YL1/2^{Fab}-EGFP (4 μg/mL)
770 under four conditions: 1) no KIF5C, 2) weakly-bound KIF5C (100 nM KIF5C, 2 mM ADP, 2 units/mL
771 hexokinase), 3) strongly-bound KIF5C (100 nM KIF5C, 6 units/mL apyrase) or 4) stepping KIF5C
772 (100 nM KIF5C, 2 mM ATP). After 3 min, the flow cell was then sealed with molten paraffin wax and
773 imaged.
774 For the washout experiments, the flow cell was infused with imaging buffer containing
775 weakly-bound KIF5C(1-560)-Halo^{554} protein (100 nM KIF5C, 2 mM ADP, 2 units/mL hexokinase) or
776 strongly-bound (apo) KIF5C(1-560)-Halo^{554} (100 nM KIF5C, 6 units/mL apyrase). After 3 min, KIF5C
777 was removed by washing the flow cell was with blocking buffer supplemented with 3 mM ATP and
778 300 mM KCl (**Supp Fig 5C,D**) based on the experiments in (Shima et al., 2018). The washing buffer
779 was immediately exchanged to imaging buffer supplemented with 52 nM YL1/2^{Fab}. The flow cell was
780 then sealed with molten paraffin wax and imaged. Fluorescence intensities along the microtubules
781 were measured using Fiji/ImageJ (width = 3 pixels), and the fluorescence intensity of an adjacent
782 region was subtracted to account for background noise.
783
784 ***Live-cell imaging of tail and lattice sensors***

785 For live cell imaging, cells were plated onto poly-D-lysine coated glass-bottom dishes 24-48
786 hr before imaging and transfected with plasmids 18-24 hr prior to imaging. HeLa stable cell lines
787 were induced for 15 hr with 2 μg/mL doxycycline prior to imaging to express superTagRFP-A1aY1 or
788 4xCAPGly-mEGFP proteins. In preparation for imaging, each dish was washed with 1 mL of warm
789 Leibovitz's L-15 Medium supplemented with 10% FBS, and 1% Penicillin-Streptomycin. Cells were
790 then incubated in imaging medium for 10 min prior to imaging.
791 To assess changes in Y-αCTT probe localization, cells exhibiting similar levels of
792 fluorescence were identified prior to imaging. Single optical sections were imaged. The localization
793 of each Y-αCTT probe was monitored before treatment and upon treatment with 10 μM Taxol or
794 0.3% DMSO (vehicle control). After 15 min, the same optical sections of each cell were imaged to
795 directly compare the localization and intensity of each probe along the microtubule lattice in a
796 compacted (before) and expanded (after) state. All cells were imaged and maintained at 37°C using
797 a DeltaVision Elite microscope system equipped with an Olympus Plan Apo N 60× 1.42 NA oil
798 immersion objective.
799 For live imaging of COS-7 cells, cells were plated onto glass-bottom dishes 48 hr prior to
800 imaging. Cells were transfected with 0.5 μg of pEGFP-N1 and 0.2 μg of Y-αCTT probe plasmid 24 hr
801 prior to imaging. Cells were transferred to warm Leibovitz's L-15 medium for imaging. Images were
802 acquired on an inverted epifluorescence microscope (Nikon TE200E) with a 60x, 1.4 NA oil-
803 immersion objective, TokaiHit stage-top incubator (INUG2A-GILCS) set to 37°C, and an Orca Flash4
804 OLT digital CMOS camera (Hamamatsu).
805
806 ***Cell fixation and immunofluorescence***
807 COS-7 cells plated onto glass coverslips were rinsed with PBS^+ (PBS with 0.9 mM $CaCl_2$,
808 0.5 mM $MgCl_2$), then fixed and permeabilized simultaneously in pre-chilled methanol (MeOH) for 10
809 min at -20°C. Cells were then either washed twice with PBS^+, rinsed with ddH_2O, dabbed on a
810 kimwipe to remove excess H_2O, and mounted onto a slide with Prolong Gold or washed twice with
811 PBS^+, blocked briefly with 0.2% fish skin gelatin (FSG) in PBS^+ and subjected to immunostaining.
812 Note that soluble EGFP used as a control in these experiments is not preserved with MeOH fixation.
813 Mouse anti-β-tubulin #E7 primary antibody was diluted in 0.2%FSG in PBS^+ and applied to cells for
814 1 hr. Cells were washed three times with 0.2% FSG in PBS^+ and then subjected to secondary
815 antibody staining for 1 hr with Alexa Fluor 680-conjugated anti-mouse in 0.2% FSG in PBS+. Finally,
816 cells were washed an additional three times with 0.2% FSG in PBS^+ and then twice with PBS^+.
817 Coverslips were dipped in ddH_2O, dabbed on a kimwipe to remove excess water, and mounted with
818 Prolong Gold.
819 HeLa cells were cultured on coverslips 24 hr prior to transfection. Approximately 20 hr post-
820 transfection, cells were fixed with methanol for 10 min at -20ºC. Following fixation, cells were
821 rehydrated in TBS supplemented with 0.1% Triton X-100 (TBS-Triton), and then blocked for 15 min
822 with 2% BSA in TBS-Triton. All primary and secondary antibodies were diluted in 2% BSA in TBS-
823 Triton. Detyrosinated microtubules were stained with a recombinant rabbit monoclonal anti-
824 detyrosinated α-tubulin antibody for 1 hr followed by anti-rabbit Alexa Fluor 594 for 30 min.
825 Overexpressed MAPs were stained with anti-GFP antibody for 1 hr, followed by anti-chicken IgY
826 Alexa Fluor 488 for 30 min. PA-tagged TubA was stained with a rat monoclonal anti-PA-tag antibody
827 for 1 hr and the anti-rat IgG Alexa Fluor 488 for 30 min. Finally, total microtubules were stained with
828 anti-α-tubulin antibody conjugated with Alexa Fluor 647 for 30 min. DNA was counterstained with
829 Hoechst, and cells were mounted with Prolong Diamond. Images were obtained with a DeltaVision
830 microscope equipped with an Olympus Plan Apo N 60x/1.42 oil immersion lens. Images were
831 subsequently deconvolved, and single optical sections are presented.
832
833 ***Quantification of αCTT probes and detyrosination in live cells***
834 Microtubule-bound A1aY1 or CAPGly sensors in Taxol-treated or TubA-expressing cells
835 were quantified as the total length of microtubule regions labeled by Y-αCTT probe per unit cell area.
836 Except for sTagRFP-A1aY1 in the Taxol treatment (see below), we measured microtubule density
837 using an image processing method developed recently (Horiuchi et al., 2025). First, to enhance the

visualized microtubule signal, raw microscopic images were subjected to 2D segmentation using a deep learning-based function in the image analysis software AIVIA. This deep learning model, based on RCA-UNet for image transformation, was trained on a dataset consisting of raw images acquired using various microtubule-targeting probes and their corresponding binarized images, in which visualized microtubule regions were manually segmented (Horiuchi et al., 2025). The enhanced images were then binarized using Otsu's thresholding in ImageJ. This segmentation process was designed to apply a strict intensity threshold, isolating high-intensity, localized binding sites from the background noise, and thus inherently excluding low-intensity binding. The binary images were subsequently skeletonized using the ImageJ plug-in Lpx_bilevelThin (Higaki et al., 2010). Cell regions were manually segmented using the Polygon Selection tool in ImageJ. Finally, microtubule density (referred to as occupancy) was calculated as the ratio of the skeletonized microtubule length to the total cell area. The final metric represents the skeletonized length of these strongly localized, high-affinity binding sites.

Microtubule-bound superTagRFP-A1aY1 sensor in the Taxol treatment experiment was quantified using Fiji Software (Schindelin et al., 2012). All images were sequentially processed using a 5-pixel rolling ball radius background subtraction, 2.0-pixel Gaussian blur, and brightness and contrast set to a minimum and maximum of 50 and 990, respectively. Images were then converted to 8-bit grayscale and microtubule-bound sensor was detected using the Fiji Ridge Detection plugin (Wagner et al., 2017) with the following settings: line width of 2.0, high contrast of 100.0, low contrast of 10.0, sigma of 1.08, lower threshold of 0.68, upper threshold of 6.97, minimum line length of 10.0, and slope method of overlap resolution. The images were binarized and total signal (IntDen) was recorded for each image and normalized to cell area.

We quantified colocalization between MAPs and Y-αCTT probes (Figure 3), or MAPs and detyrosination (Figure 4) using the threshold overlap score (TOS). This metric was calculated with the Fiji plugin EzColocalization (Stauffer et al., 2018). For analysis, TOS was determined based on the top 10th percentile of signal per cell, with cell boundaries defined manually.

To quantify microtubule detyrosination in cells expressing MAPs, we measured detyrosination signal exclusively on MAP-decorated microtubules, rather than on the entire microtubule network within the cells. Our rationale for this approach is that some MAPs exhibit localization only on specific subsets of microtubules. Therefore, measuring detyrosination against total cellular microtubules, as we performed previously (Yue et al. 2023), would inaccurately represent the net change in detyrosination directly influenced by MAP localization. To achieve this targeted measurement, we first extracted MAP-localized microtubule pixels by applying a consistent threshold across all MAP images, creating specific masks. These masks were then applied to both the total microtubule channel (visualized by anti-α-tubulin antibody DM1α) and the detyrosinated microtubule channel to obtain mean intensities for each cell. Finally, the relative intensities of detyrosination signals were plotted after normalization against the corresponding total microtubule intensities within the masked regions. In contrast, for the E254A TubA experiments, both wild-type and E254A PA-tagged TubA1A constructs showed broad incorporation into microtubules throughout the entire cell. Consequently, mean detyrosination was measured on a per-cell basis, as described previously (Yue et al. 2023).

Molecular Dynamics simulations

The starting point for our GDP simulations was the structure of the GDP-microtubule [PDB: 7SJ7 (LaFrance et al., 2022)]. To create the GTP-microtubule, we used the GMPCPP-structure [PDB: 6DPU (Zhang et al., 2018)] as a starting point, converted the GMPCPP to GTP, and fit the structure to the 7SJ7 microtubule so that it had the same lattice structure. C-terminal tails were added to every tubulin subunit. For all systems, rigid-body fitting was used to make a complete 13-protofilament, 3-start microtubule ring. This single ring was then shifted by the dimer repeat distance in order to make a 3-ring, 39-dimer microtubule fragment. For the GDP-microtubules, the 3-ring structure was converted to an "infinite" microtubule (Igaev & Grubmuller, 2020; Wells & Aksimentiev, 2010) by putting it in a periodic box where the axial length was three times the dimer repeat distance. Due to the inherent twist of the GTP-microtubule, we could not create an "infinite"

microtubule since the protofilaments would not match up with their image. Instead, the 39-dimer GTP system was solvated in a box with 20 Å padding on each side.

All systems were solvated using TIP3P water and ionized with Na+ and Cl- in order to both neutralize the system and set the ionic strength to 50 mM. Simulations were carried out using NAMD (Phillips et al., 2020) using the CHARMM36 (Best et al., 2012) force field. Following minimization and heating, we performed a short 10 ns equilibrium in an NpT ensemble with 1 atm pressure at 300 K. We then ran two independent trajectories for 260 ns and 330 ns, respectively, in the GDP-microtubule system, and one 360 ns trajectory in the GTP-microtubule system, utilizing hydrogen mass repartitioning (Hopkins et al., 2015) to allow for 4 fs time steps. All analysis was done using bio3D (Grant et al., 2006) and R (https://www.r-project.org/). Images and movies were created using VMD (Humphrey et al., 1996).

Data analysis, statistics, and presentation

All data were plotted and statistical tests were performed using GraphPad Prism (version 10.4.1; GraphPad Software). The statistical tests, sample size, and number of replicates used for each experiment are described in each figure legend. Figures were made in Adobe Illustrator 2025 (version 29.0; Adobe).

Acknowledgements:

We thank members of the Ohi, Verhey, DeSantis, Cianfrocco and Sept labs for discussions and advice. We thank Jakia Jannat Keya (University of Michigan) for purified KIF5C protein. We thank Jeff Moore (University of Colorado Anschutz Medical Center) for TubA1A plasmids and recombinant anti-TubB3 Tuj1 antibody.

Competing interests statement

The authors declare no competing interests.

Contributor Roles:

TH Investigation; Validation; Formal analysis; Visualisation; Writing – review & editing;
ECT Investigation; Validation; Formal analysis; Visualisation; Writing – review & editing;
MLP Investigation; Validation; Formal analysis; Visualisation; Writing – review & editing;
YY Investigation; Validation; Formal analysis; Visualisation; Writing – review & editing;
PD Investigation; Validation; Formal analysis; Visualisation; Writing – review & editing;
TLB Investigation; Validation; Formal analysis; Visualisation; Writing – review & editing;
MC Conceptualization; Writing – review & editing;
MD Conceptualization; Writing – review & editing;
RH Methodology; Formal analysis;
TH Methodology; Formal analysis;
DS Conceptualization; Supervision; Funding acquisition; Writing – review & editing;
RO Conceptualization; Supervision; Project administration; Funding acquisition; Writing – original draft preparation; Writing – review & editing;
KJV Conceptualization; Supervision; Project administration; Funding acquisition; Writing – original draft preparation; Writing – review & editing;

Funding information:

KJV: National Institutes of Health R35GM131744
RO: National Institutes of Health R35GM153209
ECT: Postdoctoral Fellowship PF-24-1320851-01-CCB from the American Cancer Society.
MLP: National Institutes of Health F32GM157897, Michigan Pioneer Fellows Program at the University of Michigan.
MC: National Institutes of Health R01GM141119
MD: National Institutes of Health R35GM146739
DS: National Institutes of Health R01GM136822
The funding sources were not involved in study design, data collection and interpretation, or the decision to submit the work for publication.

951 **FIGURE LEGENDS**
952
953 **Figure 1. Three probes that recognize the Y-αCTT.**
954 **(A,B)** Schematic of tubulin protein and its conformational states within the microtubule lattice.
955 (A) Schematic of tubulin heterodimer with the unstructured C-terminal tails (CTTs) protruding
956 from the body of α- and β-tubulin. (B) Tubulin adds to the end of a microtubule in a GTP-bound
957 and expanded state, resulting in a stabilizing GTP cap. In the microtubule lattice, β-tubulin
958 undergoes GTP hydrolysis, resulting in a GDP lattice and compaction of α-tubulin.
959 **(C)** Schematic of three sensors (YL1/2, A1aY1, and 4xCAP-Gly) generated to detect the
960 accessibility of the Y-αCTT along the microtubule lattice.
961 **(D,E)** Generation and validation of the YL1/2^{Fab} probe. (D) Schematic of antibody proteins.
962 YL1/2 IgG: typical mammalian IgG molecule containing two heavy (H) and two light (L) chains.
963 Light chains are comprised of one variable (V_L, light orange) and one constant (C_L, dark orange)
964 region. Heavy chains are comprised of one variable (V_H, light gray) and three constant ($C_{H1–3}$,
965 dark gray) regions. Red dots indicate complementarity determining regions (CDRs) and purple
966 lines indicate disulfide bonds. rMAb-EGFP: recombinant monoclonal antibody (rMAb) with
967 EGFP (green star) fused to the C-terminus of the light chain. YL1/2^{Fab}-EGFP: Fragment
968 antibody binding (Fab) produced from rMAb-EGFP by papain cleavage. (E) GST-tagged αCTT
969 sequences were probed by western blotting with (left) commercial YL1/2 monoclonal antibody,
970 (middle) rMAb-YL1/2-EGFP, or (right) YL1/2^{Fab}-EGFP. Each blot was also probed for GST
971 protein as a loading control. Y: full-length and tyrosinated αCTT sequence; ΔY: detyrosinated
972 αCTT sequence (lacking the C-terminal tyrosine); ΔC2: αCTT sequence lacking the C-terminal
973 two amino acids.
974 **(F)** Schematic of synthetic protein A1aY1 tagged at its N-terminus with sTag-RFP (red star).
975 **(G)** Schematic of the domain organization of (top) full-length CLIP-170 and (bottom) the
976 4xCAPGly probe tagged at its C-terminus with mEGFP (green star).
977 **(H,I)** Representative images of (H) YL1/2^{Fab}-EGFP or (I) 4xCAPGly-mEGFP proteins binding to
978 tyrosinated (Y-MT) or detyrosinated (ΔY-MT) microtubules. HeLa tubulin was polymerized into
979 microtubules and Taxol-stabilized. The microtubules were used directly (Y-MTs) or detyrosinated
980 by VASH/SVBP-containing lysate before adding the (H) YL1/2^{Fab}-EGFP or (I) 4xCAPGly-
981 mEGFP probes. Scale bars: 5 μm.
982
983 **Figure 2. Y-αCTT probes bind to the microtubule lattice after Taxol treatment.**
984 **(A-D)** Live-cell imaging of A1aY1 probe. **(A)** Representative images of the sTagRFP-A1aY1
985 HeLa stable cell line before and 15 min after treatment with (top) 0.3% DMSO control or
986 (bottom) 10 μM Taxol. Insets (boxes) show magnified views of A1aY1 probe. Scale bars: 10 μm
987 in whole-cell views and 2 μm in magnified views. **(B,C)** Quantification of probe binding to
988 microtubules. Paired data plots display the amount of A1aY1 probe bound to microtubules in
989 individual cells before and after treatment with (B) DMSO or (C) Taxol. **(D)** Mean difference plot
990 showing the fold change in A1aY1 probe binding in DMSO- vs Taxol-treated cells. DMSO=29
991 cells across 3 experiments; Taxol=59 cells across 7 experiments.
992 **(E-H)** Live-cell imaging of 4xCAPGly probe. **(E)** Representative images of the 4xCAPGly-
993 mEGFP HeLa stable cell line before and 15 minutes after treatment with (top) 0.3% DMSO

control or (bottom) 10 μM Taxol. Insets (boxes) show magnified views of CAPGly probe. Scale bars: 10 μm in whole-cell views and 2 μm in magnified views. **(F,G)** Quantification of probe binding to microtubules. Paired data plots display the amount of 4xCAPGly probe bound to microtubules in individual cells before and after treatment with (F) DMSO or (G) Taxol. **(H)** Mean difference plot showing the fold change in 4xCAPGly probe binding in DMSO- or Taxol-treated cells. DMSO=28 cells across 3 experiments; Taxol=17 cells across 5 experiments. Error bars in (D) and (H) indicate SD. ***: p<0.0002; ****: P<0.0001; ns: not significant [Student's *t* test (B,C,F,G: two-tailed; paired), (D,H: unpaired).

Figure 3. MAPs that expand the microtubule lattice increase Y-αCTT probe binding.
(A,B) Representative live-cell images of (A) A1aY1 or (B) 4xCAPGly HeLa stable cell lines transiently expressing the indicated mEGFP-tagged tubulin or MAP constructs. Cell boundaries are indicated by blue dotted lines. Scale bars: 20 μm.
(C,D) Quantification of (C) sTag-RFP-A1aY1 or (D) CAPGly-mSc3 probe colocalization with mEGFP-tagged tubulin or MAP constructs. The threshold overlap score (TOS) was measured on a per-cell basis where 1.0 indicates perfect colocalization, -1.0 indicates perfect anti-colocalization, and values near 0 indicate no relationship. Data from three independent experiments are presented as Tukey box plots. The box encompasses the 25th to 75th percentiles, with a line at the median. Whiskers show the last data point within 1.5 times the interquartile range. Outliers are plotted as individual points. *: $p < 0.1$; **: $p < 0.001$; ****: $p < 0.0001$; ns: not significant (Kruskal-Wallis test followed by post-hoc Dunn's multiple pairwise comparisons with TubA1A as the control). Number of cells analyzed (*n*) in (C): TubA1A = 69, Tau = 57, MAP2 = 66, Kif5C^{rigor} = 70, CAMSAP2 = 50, CAMSAP3 = 56, and MAP7 = 55 and in (D): TubA1A = 62, Tau = 61, MAP2 = 61, Kif5C rigor = 76, CAMSAP2 = 62, CAMSAP3 = 71, and MAP7 = 57.
(E) Schematic model depicting how expander and compactor MAPs regulate microtubule lattice conformation, influencing Y-αCTT accessibility.

Figure 4. MAPs that expand the MT lattice increase detyrosination of the Y-aCTT.
(A) Representative images of HeLa cells transiently expressing the indicated mEGFP-tagged MAPs and then fixed and stained with antibodies against detyrosinated microtubules (ΔY-tubulin) and total microtubules (MTs). Images are shown in inverted grayscale. The nuclei are represented by blue pseudocolor in the bottom panels. Blue dotted lines: boundaries of cells expressing the corresponding MAPs. Scale bars: 20 μm.
(B) Quantification of the intensity of detyrosination on MAP-bound microtubules. The fluorescence intensity of detyrosination was measured on MAP-decorated microtubules and normalized against the total microtubule intensity of MAP-decorated microtubules. Data from three independent experiments are presented as Tukey box plots. ****: $p < 0.0001$; ns: not significant (Kruskal-Wallis test followed by post-hoc Dunn's multiple pairwise comparisons with tau as the control). Number of cells analyzed (*n*): Tau = 67, MAP2 = 70, Kif5C^{rigor} = 75, CAMSAP2 = 67, CAMSAP3 = 70, and MAP7 = 67.
(C) Quantification of the colocalization of MAPs and detyrosinated microtubules. The threshold overlap score (TOS) was measured on a per-cell basis. Data from three independent experiments are presented as Tukey box plots. The box encompasses the 25th to 75th

1038 percentiles, with a line at the median. Whiskers show the last data point within 1.5 times the
1039 interquartile range. Outliers are plotted as individual points. ****: $p < 0.0001$; ns: not significant
1040 (Kruskal-Wallis test followed by post-hoc Dunn's multiple pairwise comparisons with tau as the
1041 control). Number of cells analyzed (*n*): Tau = 70, MAP2 = 72, Kif5C^{rigor} = 76, CAMSAP2 = 66,
1042 CAMSAP3 = 69, and MAP7 = 67.
1043
1044 **Figure 5. GTP-like tubulin state increases Y-αCTT accessibility and detyrosination.**
1045 **(A-D)** Live-cell imaging of Y-αCTT probes. (A,C) Representative images of (A) sTagRFP-A1aY1
1046 or (C) 4xCAPGly-mSc3 HeLa stable cell lines transiently expressing PA-tagged WT or E254A α-
1047 tubulin with an IRES-driven mEGFP protein as a reporter of transfected cells. Cell boundaries
1048 are indicated by blue dotted lines. Scale bars: 20 µm. (B,D) Quantification of (B) A1aY1 or (D)
1049 4xCAPGly probe binding to microtubules. The density was measured as the ratio of the
1050 skeletonized probe-decorated microtubule length to the total cell area. Data from three
1051 independent experiments are presented as Tukey box plots. The box encompasses the 25th to
1052 75th percentiles, with a line at the median. Whiskers show the last data point within 1.5 times
1053 the interquartile range. Outliers are plotted as individual points. **: $p < 0.01$ (Mann-Whitney U
1054 test). Number of cells analyzed (*n*) in (B): WT = 33, E254A = 29 and in (D): WT = 42, E254A =
1055 50.
1056 **(E,F)** Detyrosinated microtubules. (E) Representative images of HeLa cells transiently
1057 expressing PA-tagged WT or E254A α-tubulin (TubA1A) and then fixed and stained with
1058 antibodies against the PA tag, detyrosinated microtubules (ΔY-tubulin), and total microtubules
1059 (MTs). Images are shown in inverted grayscale. The nuclei are represented by blue pseudocolor
1060 in the bottom panels. Blue dotted lines: boundaries of cells expressing α-tubulin. Scale bars: 20
1061 µm. (F) Quantification of the intensity of detyrosination in cells expressing PA-tagged WT or
1062 E254A α-tubulin. The fluorescence intensity of detyrosination was measured on a per-cell basis
1063 and normalized against the total microtubule intensity. Data from three independent
1064 experiments are presented as Tukey box plots. ****: $p < 0.0001$; ns: not significant (Kruskal-
1065 Wallis test followed by post-hoc Dunn's multiple pairwise comparisons with the untransfected
1066 sample (untr.) as the control). Number of cells analyzed (*n*): untransfected = 105, WT = 84,
1067 E254A = 94.
1068
1069 **Figure 6. MAPs but not nucleotide state promote Y-αCTT exposure in vitro.**
1070 **(A-D)** Nucleotide state does not determine probe binding to microtubules polymerized *in vitro*.
1071 (A,C) Representative images of (A) 4xCAPGly-mEGFP or (C) YL1/2^{Fab}-GFP probe binding to a
1072 mixture containing both AlexaFluor-568 labeled GMPCPP-stabilized microtubules and
1073 AlexaFluor-647 labeled GDP microtubules. Scale bars: 5 µm. (B,D) Quantification of the
1074 fluorescence intensity of (B) 4xCAPGly-mEGFP or (D) YL1/2^{Fab}-EGFP probe binding per length
1075 of microtubule. Data are presented as scatter plots with data from three independent
1076 experiments in different shades of gray. ns: not significant (two-tailed, Student's t test).
1077 **(E-G)** Stepping KIF5C can increase YL1/2^{Fab} probe binding. (E) Flowchart of the *in vitro*
1078 reconstitution assay examining the effect of KIF5C(1-560) stepping on YL1/2^{Fab} binding. (F)
1079 Representative images of YL1/2^{Fab}-GFP probe binding to GDP-MTs in the absence or presence
1080 of KIF5C(1-560) in different nucleotide states. Scale bar: 5 µm. (G) Quantification of the mean
1081 fluorescence intensity of YL1/2^{Fab}-GFP probe along GDP-MTs under the conditions shown in

1082 (F). Each spot indicates the probe binding on an individual microtubule. Number of microtubules
1083 (n) = 74-105 from three independent experiments. ns, not significant, ****p<0.0001 (two-tailed, *t*-
1084 test).
1085
1086 **Figure 7: The nucleotide state alters Y-αCTT interactions with the microtubule body.**
1087 **(A)** Representative image from MD simulations identifying four distinct sites where the Y-αCTT
1088 interacts with the body of tubulin subunits in the microtubule: sites 1 (green) and 2 (cyan) are on
1089 the adjacent β-tubulin along a protofilament (*i.e.* next tubulin towards the microtubule minus
1090 end) whereas sites 3 (purple) and 4 (salmon) are cis-interactions with α-tubulin itself. The
1091 tubulin body is shown in cartoon and colored gray. The Y-αCTT is shown in stick and colored
1092 yellow with the aspartate and glutamate sidechains in red: 438-DSVEGEGEEEGEEY-451.
1093 **(B)** Interaction rate of the glutamate residues in the Y-αCTT with the four tubulin body sites for
1094 microtubules in the (gold) GDP or (blue) GTP states.
1095 **(C)** The fraction of Y-αCTTs that are inaccessible as a function of time for microtubules in the
1096 (gold) GDP or (blue) GTP state where inaccessibility is defined as one or more salt bridges
1097 formed between glutamates E445-E450 and the interaction sites in the microtubule body.
1098
1099 **Figure 1 – Figure Supplement 1. Recombinant YL1/2 antibody and purified probes.**
1100 **(A)** Experimentally-determined amino acid sequence YL1/2 protein. The deduced amino acid
1101 sequences of YL1/2 IgG heavy and light chains are shown. The red text indicates the
1102 complementarity determining regions (CDRs) involved in antigen recognition. Asterisks
1103 demarcate every 10 aa.
1104 **(B)** Coomassie-stained SDS-PAGE gel of purified proteins.
1105 **(C)** Validation of 4xCAPGly specificity for the Y-αCTT. GST-tagged αCTT sequences were
1106 probed by far-western blotting with purified 4xCAPGly-mEGFP protein and with an antibody
1107 against GST protein as a loading control. Y: full-length and tyrosinated αCTT sequence; ΔY:
1108 detyrosinated αCTT sequence (lacking the C-terminal tyrosine); ΔC2: αCTT sequence lacking
1109 the C-terminal two amino acids.
1110
1111 **Figure 1 – Figure Supplement 2. The A1aY1 probe must be imaged in live cells.**
1112 COS-7 cells transiently expressing sTagRFP-A1aY1 and mEGFP were (A) imaged live, (B) fixed
1113 and mounted, or (C) fixed and stained for total tubulin (microtubules). Magnified views of the red
1114 and purple boxed regions are shown to the right. Scale bars: 10 μm for whole-cell views and for
1115 magnified views.
1116
1117 **Figure 1 – Figure Supplement 3. The 4xCAPGly probe must be imaged in live cells.**
1118 COS-7 cells transiently expressing 4xCAPGly-mSc3 and mEGFP were (A) imaged live, (B) fixed
1119 and mounted, or (C) fixed and stained for total tubulin (microtubules). Magnified views of the red
1120 and purple boxed regions are shown to the right. Scale bars: 10 μm for whole-cell views and for
1121 magnified views.
1122
1123 **Figure 2 – Figure Supplement 1. Controls for probe binding in response to Taxol-**
1124 **mediated lattice expansion.**

1125 **(A,B)** Y-αCTT probes bind to the microtubule lattice after Taxol-induced expansion.
1126 Representative images of (A) sTagRFP-A1aY1 or (B) 4xCAPGly-mEGFP probes transiently
1127 expressed in (top) HeLa or (bottom) COS-7 cells and imaged live before or 15 min after addition
1128 of 10 μM Taxol. Scale bars: 10 μm.
1129 **(C)** EB3-EGFP is rapidly evicted from microtubules after Taxol addition. HeLa cells stably expressing
1130 EB3-EGFP were imaged live before (0 min) and at the indicated time points after addition of 2 μM
1131 Taxol. Scale bar: 10 μm.
1132
1133 **Figure 5 – Figure Supplement 1. Controls for nucleotide-mediated lattice expansion.**
1134 **(A,B)** Western blot of HeLa cells transiently expressing internal PA-tagged α-tubulin TubA1A.
1135 (A) sTagRFP-A1aY1 stable HeLa cells or (B) 4xCAPGly-mSc3 stable HeLa cells were untransfected
1136 (untr.) or transfected with plasmids for expressing PA-tagged WT or E254A α-tubulin (TubA1A).
1137 Whole cell lysates were prepared and analyzed by immunoblotting with the antibodies indicated on
1138 the left side of the blots. Size markers in kD are indicated on the right side of the blots. Asterisks
1139 denote upshifted PA-tagged tubulin bands.
1140
1141 **Figure 6 – Figure Supplement 1. Controls for washout of strongly-bound (apo) KIF5C.**
1142 **(A,B)** Wash out of strongly-bound (apo) KIF5C. (A) Representative images of KIF5C(1-560)-
1143 Halo^{554} binding to GDP-MTs in ATP (stepping) or no nucleotide (apo) conditions. In the wash out
1144 condition, strongly-bound (apo) KIF5C was released from the microtubules by washing the flow
1145 chamber with buffer containing 3 mM ATP and 300 mM KCl. Scale bar: 5 μm. (B) Quantification
1146 of the mean fluorescence intensity of KIF5C(1-560)-Halo^{554} along GDP-MTs under the
1147 conditions shown in (A). Each spot indicates KIF5C(1-560)-Halo^{554} fluorescence intensity on an
1148 individual microtubule. Number of microtubules (n) = 24-46 from two independent experiments.
1149 ****$p<0.0001$ (two-tailed, t-test).
1150
1151 **Figure 7 – Figure Supplement 1. The Y-αCTT primarily contacts four sites in the tubulin**
1152 **body within a GDP microtubule lattice.**
1153 Jaccard index plot indicating the frequency of two residues simultaneously forming salt bridges
1154 with the Y-αCTT based on molecular dynamics simulations of a GDP microtubule lattice**.** The
1155 scale represents the Jaccard index where an index of 0 indicates that the two residues are
1156 never interacting with the Y-αCTT at the same time and an index of 1 indicates that when one of
1157 the two residues is interacting with the Y-αCTT, the other is also interacting with the Y-αCTT.
1158
1159 **Video 1. Movie of Y-αCTT interacting with the tubulin body from molecular dynamics**
1160 **(MD) simulations.**
1161 Representative movie from MD simulations showing interactions of the Y-αCTT with the tubulin
1162 body over 240 ns. The tubulin body is shown in cartoon and colored gray. The αCTT is shown in
1163 stick and colored yellow with the glutamate sidechains in red. Residues in site 1 (green), site 2
1164 (cyan), and site 3 (magenta) appear as spheres when the αCTT is forming salt bridges with
1165 those residues.
1166
1167

REFERENCES

Alushin, G. M., Lander, G. C., Kellogg, E. H., Zhang, R., Baker, D., & Nogales, E. (2014). High-resolution microtubule structures reveal the structural transitions in alphabeta-tubulin upon GTP hydrolysis. *Cell*, *157*(5), 1117-1129. https://doi.org/10.1016/j.cell.2014.03.053

Arnal, I., Heichette, C., Diamantopoulos, G. S., & Chretien, D. (2004). CLIP-170/tubulin-curved oligomers coassemble at microtubule ends and promote rescues. *Curr Biol*, *14*(23), 2086-2095. https://doi.org/10.1016/j.cub.2004.11.055

Beckett, D., & Voth, G. A. (2023). Unveiling the catalytic mechanism of GTP hydrolysis in microtubules. *Proc Natl Acad Sci U S A*, *120*(27), e2305899120. https://doi.org/10.1073/pnas.2305899120

Benkirane, M., Bonhomme, M., Morsy, H., Safgren, S. L., Marelli, C., Chaussenot, A., Smedley, D., Cipriani, V., de Sainte-Agathe, J. M., Ding, C., Larrieu, L., Vestito, L., Margot, H., Lesca, G., Ramond, F., Castrioto, A., Baux, D., Verheijen, J., Sansa, E.,…Koenig, M. (2024). De novo and inherited monoallelic variants in TUBA4A cause ataxia and spasticity. *Brain*, *147*(11), 3681-3689. https://doi.org/10.1093/brain/awae193

Best, R. B., Zhu, X., Shim, J., Lopes, P. E., Mittal, J., Feig, M., & Mackerell, A. D., Jr. (2012). Optimization of the additive CHARMM all-atom protein force field targeting improved sampling of the backbone phi, psi and side-chain chi(1) and chi(2) dihedral angles. *J Chem Theory Comput*, *8*(9), 3257-3273. https://doi.org/10.1021/ct300400x

Bieling, P., Kandels-Lewis, S., Telley, I. A., van Dijk, J., Janke, C., & Surrey, T. (2008). CLIP-170 tracks growing microtubule ends by dynamically recognizing composite EB1/tubulin-binding sites. *J Cell Biol*, *183*(7), 1223-1233. https://doi.org/10.1083/jcb.200809190

Bodey, A. J., Kikkawa, M., & Moores, C. A. (2009). 9-Angstrom structure of a microtubule-bound mitotic motor. *J Mol Biol*, *388*(2), 218-224. https://doi.org/10.1016/j.jmb.2009.03.008

Castle, B. T., McKibben, K. M., Rhoades, E., & Odde, D. J. (2020). Tau Avoids the GTP Cap at Growing Microtubule Plus-Ends. *iScience*, *23*(12), 101782. https://doi.org/10.1016/j.isci.2020.101782

Chaudhary, A. R., Lu, H., Krementsova, E. B., Bookwalter, C. S., Trybus, K. M., & Hendricks, A. G. (2019). MAP7 regulates organelle transport by recruiting kinesin-1 to microtubules. *J Biol Chem*, *294*(26), 10160-10171. https://doi.org/10.1074/jbc.RA119.008052

Chew, Y. M., & Cross, R. A. (2023). Taxol acts differently on different tubulin isotypes. *Commun Biol*, *6*(1), 946. https://doi.org/10.1038/s42003-023-05306-y

Chew, Y. M., & Cross, R. A. (2025). Structural switching of tubulin in the microtubule lattice. *Biochem Soc Trans*, *53*(1). https://doi.org/10.1042/BST20240360

Chothia, C., & Lesk, A. M. (1987). Canonical structures for the hypervariable regions of immunoglobulins. *J Mol Biol*, *196*(4), 901-917. https://doi.org/10.1016/0022-2836(87)90412-8

Cleary, J. M., & Hancock, W. O. (2021). Molecular mechanisms underlying microtubule growth dynamics. *Curr Biol*, *31*(10), R560-R573. https://doi.org/10.1016/j.cub.2021.02.035

de Jager, L., Jansen, K. I., Hoogebeen, R., Akhmanova, A., Kapitein, L. C., Forster, F., & Howes, S. C. (2025). StableMARK-decorated microtubules in cells have expanded lattices. *J Cell Biol*, *224*(1), e202206143. https://doi.org/10.1083/jcb.202206143

Diggle, C. P., Martinez-Garay, I., Molnar, Z., Brinkworth, M. H., White, E., Fowler, E., Hughes, R., Hayward, B. E., Carr, I. M., Watson, C. M., Crinnion, L., Asipu, A., Woodman, B., Coletta, P. L., Markham, A. F., Dear, T. N., Bonthron, D. T., Peckham, M., Morrison, E. E., & Sheridan, E. (2017). A tubulin alpha 8 mouse knockout model indicates a likely role in spermatogenesis but not in brain development. *PLoS One*, *12*(4), e0174264. https://doi.org/10.1371/journal.pone.0174264

Ebberink, E., Fernandes, S., Hatzopoulos, G., Agashe, N., Chang, P. H., Guidotti, N., Reichart, T. M., Reymond, L., Velluz, M. C., Schneider, F., Pourroy, C., Janke, C., Gonczy, P., Fierz, B., & Aumeier, C. (2023). Tubulin engineering by semi-synthesis reveals that polyglutamylation directs detyrosination. *Nat Chem*, *15*(8), 1179-1187. https://doi.org/10.1038/s41557-023-01228-8

Egoldt, C., Velluz, M.-C., Tran, J., & Aumeier, C. (2025). Microtubule lattice conformation and integrity regulate α-tubulin acetylation. *bioRxiv,* 2025.09.09.675099. https://doi.org/10.1101/2025.09.09.675099

Estevez-Gallego, J., Blum, T. B., Ruhnow, F., Gili, M., Speroni, S., Garcia-Castellanos, R., Steinmetz, M. O., & Surrey, T. (2025). Hydrolysis-deficient mosaic microtubules as faithful mimics of the GTP cap. *Nat Commun*, *16*(1), 2396. https://doi.org/10.1038/s41467-025-57555-6

Estevez-Gallego, J., Josa-Prado, F., Ku, S., Buey, R. M., Balaguer, F. A., Prota, A. E., Lucena-Agell, D., Kamma-Lorger, C., Yagi, T., Iwamoto, H., Duchesne, L., Barasoain, I., Steinmetz, M. O., Chretien, D., Kamimura, S., Diaz, J. F., & Oliva, M. A. (2020). Structural model for differential cap maturation at growing microtubule ends. *Elife*, *9,* e50155. https://doi.org/10.7554/eLife.50155

Fan, X., & McKenney, R. J. (2023). Control of motor landing and processivity by the CAP-Gly domain in the KIF13B tail. *Nat Commun*, *14*(1), 4715. https://doi.org/10.1038/s41467-023-40425-4

Ferro, L. S., Fang, Q., Eshun-Wilson, L., Fernandes, J., Jack, A., Farrell, D. P., Golcuk, M., Huijben, T., Costa, K., Gur, M., DiMaio, F., Nogales, E., & Yildiz, A. (2022). Structural and functional insight into regulation of kinesin-1 by microtubule-associated protein MAP7. *Science*, *375*(6578), 326-331. https://doi.org/10.1126/science.abf6154

Forth, S., & Kapoor, T. M. (2017). The mechanics of microtubule networks in cell division. *J Cell Biol*, *216*(6), 1525-1531. https://doi.org/10.1083/jcb.201612064

Fourriere, L., Jimenez, A. J., Perez, F., & Boncompain, G. (2020). The role of microtubules in secretory protein transport. *J Cell Sci*, *133*(2), jcs237016. https://doi.org/10.1242/jcs.237016

Freedman, H., Luchko, T., Luduena, R. F., & Tuszynski, J. A. (2011). Molecular dynamics modeling of tubulin C-terminal tail interactions with the microtubule surface. *Proteins*, *79*(10), 2968-2982. https://doi.org/10.1002/prot.23155

Gadella, T. W. J., Jr., van Weeren, L., Stouthamer, J., Hink, M. A., Wolters, A. H. G., Giepmans, B. N. G., Aumonier, S., Dupuy, J., & Royant, A. (2023). mScarlet3: a brilliant and fast-maturing red fluorescent protein. *Nat Methods*, *20*(4), 541-545. https://doi.org/10.1038/s41592-023-01809-y

Grant, B. J., Rodrigues, A. P., ElSawy, K. M., McCammon, J. A., & Caves, L. S. (2006). Bio3d: an R package for the comparative analysis of protein structures. *Bioinformatics*, *22*(21), 2695-2696. https://doi.org/10.1093/bioinformatics/btl461

Gudimchuk, N. B., & McIntosh, J. R. (2021). Regulation of microtubule dynamics, mechanics and function through the growing tip. *Nat Rev Mol Cell Biol*, *22*(12), 777-795. https://doi.org/10.1038/s41580-021-00399-x

Hausrat, T. J., Radwitz, J., Lombino, F. L., Breiden, P., & Kneussel, M. (2021). Alpha- and beta-tubulin isotypes are differentially expressed during brain development. *Dev Neurobiol*, *81*(3), 333-350. https://doi.org/10.1002/dneu.22745

Higaki, T., Kutsuna, N., Sano, T., Kondo, N., & Hasezawa, S. (2010). Quantification and cluster analysis of actin cytoskeletal structures in plant cells: role of actin bundling in stomatal movement during diurnal cycles in Arabidopsis guard cells. *Plant J*, *61*(1), 156-165. https://doi.org/10.1111/j.1365-313x.2009.04032.x

Honnappa, S., Okhrimenko, O., Jaussi, R., Jawhari, H., Jelesarov, I., Winkler, F. K., & Steinmetz, M. O. (2006). Key interaction modes of dynamic +TIP networks. *Mol Cell*, *23*(5), 663-671. https://doi.org/10.1016/j.molcel.2006.07.013

Hooikaas, P. J., Martin, M., Muhlethaler, T., Kuijntjes, G. J., Peeters, C. A. E., Katrukha, E. A., Ferrari, L., Stucchi, R., Verhagen, D. G. F., van Riel, W. E., Grigoriev, I., Altelaar, A. F. M., Hoogenraad, C. C., Rudiger, S. G. D., Steinmetz, M. O., Kapitein, L. C., & Akhmanova, A. (2019). MAP7 family proteins regulate kinesin-1 recruitment and activation. *J Cell Biol*, *218*(4), 1298-1318. https://doi.org/10.1083/jcb.201808065

Hopkins, C. W., Le Grand, S., Walker, R. C., & Roitberg, A. E. (2015). Long-Time-Step Molecular Dynamics through Hydrogen Mass Repartitioning. *J Chem Theory Comput*, *11*(4), 1864-1874. https://doi.org/10.1021/ct5010406

Horiuchi, R., Kamimura, A., Hanaki, Y., Matsumoto, H., Ueda, M., & Higaki, T. (2025). Deep learning-based cytoskeleton segmentation for accurate high-throughput measurement of cytoskeleton density. *Protoplasma*, *262*(3), 739-751. https://doi.org/10.1007/s00709-024-02019-9

Hotta, T., McAlear, T. S., Yue, Y., Higaki, T., Haynes, S. E., Nesvizhskii, A. I., Sept, D., Verhey, K. J., Bechstedt, S., & Ohi, R. (2022). EML2-S constitutes a new class of proteins that recognizes and regulates the dynamics of tyrosinated microtubules. *Curr Biol*, *32*(18), 3898-3910. https://doi.org/10.1016/j.cub.2022.07.027

Hotta, T., Plemmons, A., Gebbie, M., Ziehm, T. A., Blasius, T. L., Johnson, C., Verhey, K. J., Pearring, J. N., & Ohi, R. (2023). Mechanistic Analysis of CCP1 in Generating DeltaC2 alpha-Tubulin in

Mammalian Cells and Photoreceptor Neurons. *Biomolecules*, *13*(2), 357. https://doi.org/10.3390/biom13020357

Howes, S. C., Geyer, E. A., LaFrance, B., Zhang, R., Kellogg, E. H., Westermann, S., Rice, L. M., & Nogales, E. (2017). Structural differences between yeast and mammalian microtubules revealed by cryo-EM. *J Cell Biol*, *216*(9), 2669-2677. https://doi.org/10.1083/jcb.201612195

Hughes, S. M. (1983). Are guanine nucleotide binding proteins a distinct class of regulatory proteins? *FEBS Lett*, *164*(1), 1-8. https://doi.org/10.1016/0014-5793(83)80006-4

Humphrey, W., Dalke, A., & Schulten, K. (1996). VMD: visual molecular dynamics. *J Mol Graph*, *14*(1), 33-38, 27-38. https://doi.org/10.1016/0263-7855(96)00018-5

Igaev, M., & Grubmuller, H. (2020). Microtubule instability driven by longitudinal and lateral strain propagation. *PLoS Comput Biol*, *16*(9), e1008132. https://doi.org/10.1371/journal.pcbi.1008132

Janke, C., & Magiera, M. M. (2020). The tubulin code and its role in controlling microtubule properties and functions. *Nat Rev Mol Cell Biol*, *21*(6), 307-326. https://doi.org/10.1038/s41580-020-0214-3

Kellogg, E. H., Hejab, N. M. A., Howes, S., Northcote, P., Miller, J. H., Diaz, J. F., Downing, K. H., & Nogales, E. (2017). Insights into the Distinct Mechanisms of Action of Taxane and Non-Taxane Microtubule Stabilizers from Cryo-EM Structures. *J Mol Biol*, *429*(5), 633-646. https://doi.org/10.1016/j.jmb.2017.01.001

Kesarwani, S., Lama, P., Chandra, A., Reddy, P. P., Jijumon, A. S., Bodakuntla, S., Rao, B. M., Janke, C., Das, R., & Sirajuddin, M. (2020). Genetically encoded live-cell sensor for tyrosinated microtubules. *J Cell Biol*, *219*(10), e201912107. https://doi.org/10.1083/jcb.201912107

Khandelia, P., Yap, K., & Makeyev, E. V. (2011). Streamlined platform for short hairpin RNA interference and transgenesis in cultured mammalian cells. *Proc Natl Acad Sci U S A*, *108*(31), 12799-12804. https://doi.org/10.1073/pnas.1103532108

Kilmartin, J. V., Wright, B., & Milstein, C. (1982). Rat monoclonal antitubulin antibodies derived by using a new nonsecreting rat cell line. *J Cell Biol*, *93*(3), 576-582. https://doi.org/10.1083/jcb.93.3.576

LaFrance, B. J., Roostalu, J., Henkin, G., Greber, B. J., Zhang, R., Normanno, D., McCollum, C. O., Surrey, T., & Nogales, E. (2022). Structural transitions in the GTP cap visualized by cryo-electron microscopy of catalytically inactive microtubules. *Proc Natl Acad Sci U S A*, *119*(2), e2114994119. https://doi.org/10.1073/pnas.2114994119

Laurin, Y., Eyer, J., Robert, C. H., Prevost, C., & Sacquin-Mora, S. (2017). Mobility and Core-Protein Binding Patterns of Disordered C-Terminal Tails in beta-Tubulin Isotypes. *Biochemistry*, *56*(12), 1746-1756. https://doi.org/10.1021/acs.biochem.6b00988

Lindsay, K. A., Abdelhamid, N., Kahawatte, S., Dima, R. I., Sackett, D. L., Finegan, T. M., & Ross, J. L. (2023). A Tale of 12 Tails: Katanin Severing Activity Affected by Carboxy-Terminal Tail Sequences. *Biomolecules*, *13*(4), 620. https://doi.org/10.3390/biom13040620

Liu, H., & Shima, T. (2023). Preference of CAMSAP3 for expanded microtubule lattice contributes to stabilization of the minus end. *Life Sci Alliance*, *6*(5), e202201714. https://doi.org/10.26508/lsa.202201714

Logan, C. M., & Menko, A. S. (2019). Microtubules: Evolving roles and critical cellular interactions. *Exp Biol Med (Maywood)*, *244*(15), 1240-1254. https://doi.org/10.1177/1535370219867296

Luchko, T., Huzil, J. T., Stepanova, M., & Tuszynski, J. (2008). Conformational analysis of the carboxy-terminal tails of human beta-tubulin isotypes. *Biophys J*, *94*(6), 1971-1982. https://doi.org/10.1529/biophysj.107.115113

Manka, S. W., & Moores, C. A. (2018). Microtubule structure by cryo-EM: snapshots of dynamic instability. *Essays Biochem*, *62*(6), 737-751. https://doi.org/10.1042/EBC20180031

McKenney, R. J., Huynh, W., Vale, R. D., & Sirajuddin, M. (2016). Tyrosination of alpha-tubulin controls the initiation of processive dynein-dynactin motility. *EMBO J*, *35*(11), 1175-1185. https://doi.org/10.15252/embj.201593071

Metivier, M., Monroy, B. Y., Gallaud, E., Caous, R., Pascal, A., Richard-Parpaillon, L., Guichet, A., Ori-McKenney, K. M., & Giet, R. (2019). Dual control of Kinesin-1 recruitment to microtubules by Ensconsin in Drosophila neuroblasts and oocytes. *Development*, *146*(8), dev171579. https://doi.org/10.1242/dev.171579

Mishima, M., Maesaki, R., Kasa, M., Watanabe, T., Fukata, M., Kaibuchi, K., & Hakoshima, T. (2007). Structural basis for tubulin recognition by cytoplasmic linker protein 170 and its autoinhibition. *Proc Natl Acad Sci U S A*, *104*(25), 10346-10351. https://doi.org/10.1073/pnas.0703876104

Mitchison, T., & Kirschner, M. (1984). Dynamic instability of microtubule growth. *Nature*, *312*(5991), 237-242. https://doi.org/10.1038/312237a0

Mo, G. C. H., Posner, C., Rodriguez, E. A., Sun, T., & Zhang, J. (2020). A rationally enhanced red fluorescent protein expands the utility of FRET biosensors. *Nat Commun*, *11*(1), 1848. https://doi.org/10.1038/s41467-020-15687-x

Monroy, B. Y., Tan, T. C., Oclaman, J. M., Han, J. S., Simo, S., Niwa, S., Nowakowski, D. W., McKenney, R. J., & Ori-McKenney, K. M. (2020). A Combinatorial MAP Code Dictates Polarized Microtubule Transport. *Dev Cell*, *53*(1), 60-72. https://doi.org/10.1016/j.devcel.2020.01.029

Muto, E., Sakai, H., & Kaseda, K. (2005). Long-range cooperative binding of kinesin to a microtubule in the presence of ATP. *J Cell Biol*, *168*(5), 691-696. https://doi.org/10.1083/jcb.200409035

Nicot, S., Gillard, G., Impheng, H., Joachimiak, E., Urbach, S., Mochizuki, K., Wloga, D., Juge, F., & Rogowski, K. (2023). A family of carboxypeptidases catalyzing alpha- and beta-tubulin tail processing and deglutamylation. *Sci Adv*, *9*(37), eadi7838. https://doi.org/10.1126/sciadv.adi7838

Niederstrasser, H., Salehi-Had, H., Gan, E. C., Walczak, C., & Nogales, E. (2002). XKCM1 acts on a single protofilament and requires the C terminus of tubulin. *J Mol Biol*, *316*(3), 817-828. https://doi.org/10.1006/jmbi.2001.5360

Nogales, E., Downing, K. H., Amos, L. A., & Lowe, J. (1998). Tubulin and FtsZ form a distinct family of GTPases. *Nat Struct Biol*, *5*(6), 451-458. https://doi.org/10.1038/nsb0698-451

Pan, X., Cao, Y., Stucchi, R., Hooikaas, P. J., Portegies, S., Will, L., Martin, M., Akhmanova, A., Harterink, M., & Hoogenraad, C. C. (2019). MAP7D2 Localizes to the Proximal Axon and Locally Promotes Kinesin-1-Mediated Cargo Transport into the Axon. *Cell Rep*, *26*(8), 1988-1999. https://doi.org/10.1016/j.celrep.2019.01.084

Paquette, A. L., Tetlalmatzi, S. C., Haineault, J. A. G., Li, Y., Finkel, N., Hendricks, A. G., Brouhard, G. J., & Sebastien, M. (2025). Competition for microtubule lattice spacing between a microtubule expander and compactor. *Curr Biol*, *35*(18), 4442-4452. https://doi.org/10.1016/j.cub.2025.07.080

Peet, D. R., Burroughs, N. J., & Cross, R. A. (2018). Kinesin expands and stabilizes the GDP-microtubule lattice. *Nat Nanotechnol*, *13*(5), 386-391. https://doi.org/10.1038/s41565-018-0084-4

Peris, L., Thery, M., Faure, J., Saoudi, Y., Lafanechere, L., Chilton, J. K., Gordon-Weeks, P., Galjart, N., Bornens, M., Wordeman, L., Wehland, J., Andrieux, A., & Job, D. (2006). Tubulin tyrosination is a major factor affecting the recruitment of CAP-Gly proteins at microtubule plus ends. *J Cell Biol*, *174*(6), 839-849. https://doi.org/10.1083/jcb.200512058

Phillips, J. C., Hardy, D. J., Maia, J. D. C., Stone, J. E., Ribeiro, J. V., Bernardi, R. C., Buch, R., Fiorin, G., Henin, J., Jiang, W., McGreevy, R., Melo, M. C. R., Radak, B. K., Skeel, R. D., Singharoy, A., Wang, Y., Roux, B., Aksimentiev, A., Luthey-Schulten, Z.,…Tajkhorshid, E. (2020). Scalable molecular dynamics on CPU and GPU architectures with NAMD. *J Chem Phys*, *153*(4), 044130. https://doi.org/10.1063/5.0014475

Prosser, S. L., & Pelletier, L. (2017). Mitotic spindle assembly in animal cells: a fine balancing act. *Nat Rev Mol Cell Biol*, *18*(3), 187-201. https://doi.org/10.1038/nrm.2016.162

Prota, A. E., Lucena-Agell, D., Ma, Y., Estevez-Gallego, J., Li, S., Bargsten, K., Josa-Prado, F., Altmann, K. H., Gaillard, N., Kamimura, S., Muhlethaler, T., Gago, F., Oliva, M. A., Steinmetz, M. O., Fang, W. S., & Diaz, J. F. (2023). Structural insight into the stabilization of microtubules by taxanes. *Elife*, *12,* e84791. https://doi.org/10.7554/eLife.84791

Risteski, P., Jagric, M., Pavin, N., & Tolic, I. M. (2021). Biomechanics of chromosome alignment at the spindle midplane. *Curr Biol*, *31*(10), R574-R585. https://doi.org/10.1016/j.cub.2021.03.082

Roll-Mecak, A. (2020). The Tubulin Code in Microtubule Dynamics and Information Encoding. *Dev Cell*, *54*(1), 7-20. https://doi.org/10.1016/j.devcel.2020.06.008

Roostalu, J., Thomas, C., Cade, N. I., Kunzelmann, S., Taylor, I. A., & Surrey, T. (2020). The speed of GTP hydrolysis determines GTP cap size and controls microtubule stability. *Elife*, *9, e51992*. https://doi.org/10.7554/eLife.51992

Sahoo, A., & Hanson, S. M. (2025). Microtubules in Martini: Parameterizing a heterogeneous elastic-network towards a mechanically accurate microtubule. *PNAS Nexus*, *4*(7), pgaf202. https://doi.org/10.1093/pnasnexus/pgaf202

Scheel, J., Pierre, P., Rickard, J. E., Diamantopoulos, G. S., Valetti, C., van der Goot, F. G., Haner, M., Aebi, U., & Kreis, T. E. (1999). Purification and analysis of authentic CLIP-170 and recombinant fragments. *J Biol Chem*, *274*(36), 25883-25891. https://doi.org/10.1074/jbc.274.36.25883

Schindelin, J., Arganda-Carreras, I., Frise, E., Kaynig, V., Longair, M., Pietzsch, T., Preibisch, S., Rueden, C., Saalfeld, S., Schmid, B., Tinevez, J. Y., White, D. J., Hartenstein, V., Eliceiri, K., Tomancak, P., & Cardona, A. (2012). Fiji: an open-source platform for biological-image analysis. *Nat Methods*, *9*(7), 676-682. https://doi.org/10.1038/nmeth.2019

Serrano, L., Avila, J., & Maccioni, R. B. (1984). Controlled proteolysis of tubulin by subtilisin: localization of the site for MAP2 interaction. *Biochemistry*, *23*(20), 4675-4681. https://doi.org/10.1021/bi00315a024

Serrano, L., de la Torre, J., Maccioni, R. B., & Avila, J. (1984). Involvement of the carboxyl-terminal domain of tubulin in the regulation of its assembly. *Proc Natl Acad Sci U S A*, *81*(19), 5989-5993. https://doi.org/10.1073/pnas.81.19.5989

Serrano, L., Montejo de Garcini, E., Hernandez, M. A., & Avila, J. (1985). Localization of the tubulin binding site for tau protein. *Eur J Biochem*, *153*(3), 595-600. https://doi.org/10.1111/j.1432-1033.1985.tb09342.x

Shen, Y., & Ori-McKenney, K. M. (2024). Microtubule-associated protein MAP7 promotes tubulin posttranslational modifications and cargo transport to enable osmotic adaptation. *Dev Cell*, *59*(12), 1553-1570. https://doi.org/10.1016/j.devcel.2024.03.022

Shima, T., Morikawa, M., Kaneshiro, J., Kambara, T., Kamimura, S., Yagi, T., Iwamoto, H., Uemura, S., Shigematsu, H., Shirouzu, M., Ichimura, T., Watanabe, T. M., Nitta, R., Okada, Y., & Hirokawa, N. (2018). Kinesin-binding-triggered conformation switching of microtubules contributes to polarized transport. *J Cell Biol*, *217*(12), 4164-4183. https://doi.org/10.1083/jcb.201711178

Siahaan, V., Tan, R., Humhalova, T., Libusova, L., Lacey, S. E., Tan, T., Dacy, M., Ori-McKenney, K. M., McKenney, R. J., Braun, M., & Lansky, Z. (2022). Microtubule lattice spacing governs cohesive envelope formation of tau family proteins. *Nat Chem Biol*, *18*(11), 1224-1235. https://doi.org/10.1038/s41589-022-01096-2

Souphron, J., Bodakuntla, S., Jijumon, A. S., Lakisic, G., Gautreau, A. M., Janke, C., & Magiera, M. M. (2019). Purification of tubulin with controlled post-translational modifications by polymerization-depolymerization cycles. *Nat Protoc*, *14*(5), 1634-1660. https://doi.org/10.1038/s41596-019-0153-7

Stauffer, W., Sheng, H., & Lim, H. N. (2018). EzColocalization: An ImageJ plugin for visualizing and measuring colocalization in cells and organisms. *Sci Rep*, *8*(1), 15764. https://doi.org/10.1038/s41598-018-33592-8

Thomas, E. C., Yue, Y., Pimm, M. L., Hotta, T., Ohi, R., & Verhey, K. J. (2025). Purification, fluorescent labelling, and detyrosination of mammalian cell tubulin for biochemical assays. *Cytoskeleton Jul 12*:10.1002/cm.70005 https://doi.org/10.1002/cm.70005.

Tymanskyj, S. R., Yang, B. H., Verhey, K. J., & Ma, L. (2018). MAP7 regulates axon morphogenesis by recruiting kinesin-1 to microtubules and modulating organelle transport. *Elife*, *7, e36374*. https://doi.org/10.7554/eLife.36374

Verhey, K. J., & Ohi, R. (2023). Causes, costs and consequences of kinesin motors communicating through the microtubule lattice. *J Cell Sci*, *136*(5), jcs260735. https://doi.org/10.1242/jcs.260735

Wagner, T., Hiner, M., & xraynaud. (2017). Ridge Detection 1.4.0. *Zenodo*. https://doi.org/https://doi.org/10.5281/zenodo.845874

Wall, K. P., Pagratis, M., Armstrong, G., Balsbaugh, J. L., Verbeke, E., Pearson, C. G., & Hough, L. E. (2016). Molecular Determinants of Tubulin's C-Terminal Tail Conformational Ensemble. *ACS Chem Biol*, *11*(11), 2981-2990. https://doi.org/10.1021/acschembio.6b00507

Wang, Z., & Sheetz, M. P. (2000). The C-terminus of tubulin increases cytoplasmic dynein and kinesin processivity. *Biophys J*, *78*(4), 1955-1964. https://doi.org/10.1016/S0006-3495(00)76743-9

Wehland, J., Henkart, M., Klausner, R., & Sandoval, I. V. (1983). Role of microtubules in the distribution of the Golgi apparatus: effect of taxol and microinjected anti-alpha-tubulin antibodies. *Proc Natl Acad Sci U S A*, *80*(14), 4286-4290. https://doi.org/10.1073/pnas.80.14.4286

Weisbrich, A., Honnappa, S., Jaussi, R., Okhrimenko, O., Frey, D., Jelesarov, I., Akhmanova, A., & Steinmetz, M. O. (2007). Structure-function relationship of CAP-Gly domains. *Nat Struct Mol Biol*, *14*(10), 959-967. https://doi.org/10.1038/nsmb1291

Wells, D. B., & Aksimentiev, A. (2010). Mechanical properties of a complete microtubule revealed through molecular dynamics simulation. *Biophys J*, *99*(2), 629-637. https://doi.org/10.1016/j.bpj.2010.04.038

Wijeratne, S. S., Fiorenza, S. A., Neary, A. E., Subramanian, R., & Betterton, M. D. (2022). Motor guidance by long-range communication on the microtubule highway. *Proc Natl Acad Sci U S A*, *119*(28), e2120193119. https://doi.org/10.1073/pnas.2120193119

Yue, Y., Hotta, T., Higaki, T., Verhey, K. J., & Ohi, R. (2023). Microtubule detyrosination by VASH1/SVBP is regulated by the conformational state of tubulin in the lattice. *Curr Biol*, *33*(19), 4111-4123 e4117. https://doi.org/10.1016/j.cub.2023.07.062

Yue, Y., Hotta, T., Ohi, R., & Verhey, K. J. (2025). MATCAP1 preferentially binds an expanded tubulin conformation to generate detyrosinated and ΔC2 α-tubulin. *bioRxiv*. 2025.08.14.670257. https://doi.org/10.1101/2025.08.14.670257

Zehr, E. A., & Roll-Mecak, A. (2023). Cryo-EM structures of human α1B/βI+βIVb microtubules shed light on isoform specific assembly. *bioRxiv*. 2023.12.01.569594. https://doi.org/10.1101/2023.12.01.569594

Zehr, E. A., Szyk, A., Szczesna, E., & Roll-Mecak, A. (2020). Katanin Grips the beta-Tubulin Tail through an Electropositive Double Spiral to Sever Microtubules. *Dev Cell*, *52*(1), 118-131. https://doi.org/10.1016/j.devcel.2019.10.010

Zhang, R., LaFrance, B., & Nogales, E. (2018). Separating the effects of nucleotide and EB binding on microtubule structure. *Proc Natl Acad Sci U S A*, *115*(27), E6191-E6200. https://doi.org/10.1073/pnas.1802637115

Zhokhov, S. S., Kovalyov, S. V., Samgina, T. Y., & Lebedev, A. T. (2017). An EThcD-Based Method for Discrimination of Leucine and Isoleucine Residues in Tryptic Peptides. *J Am Soc Mass Spectrom*, *28*(8), 1600-1611. https://doi.org/10.1007/s13361-017-1674-3

Zhu, Z., Ashrafian, H., Tabrizi, N. M., Matas, E., Girard, L., Ma, H., & Nice, E. C. (2025). Antibody numbering schemes: advances, comparisons and tools for antibody engineering. *Protein Eng Des Sel*, *38, 2023.12.01.569594*. https://doi.org/10.1093/protein/gzaf005

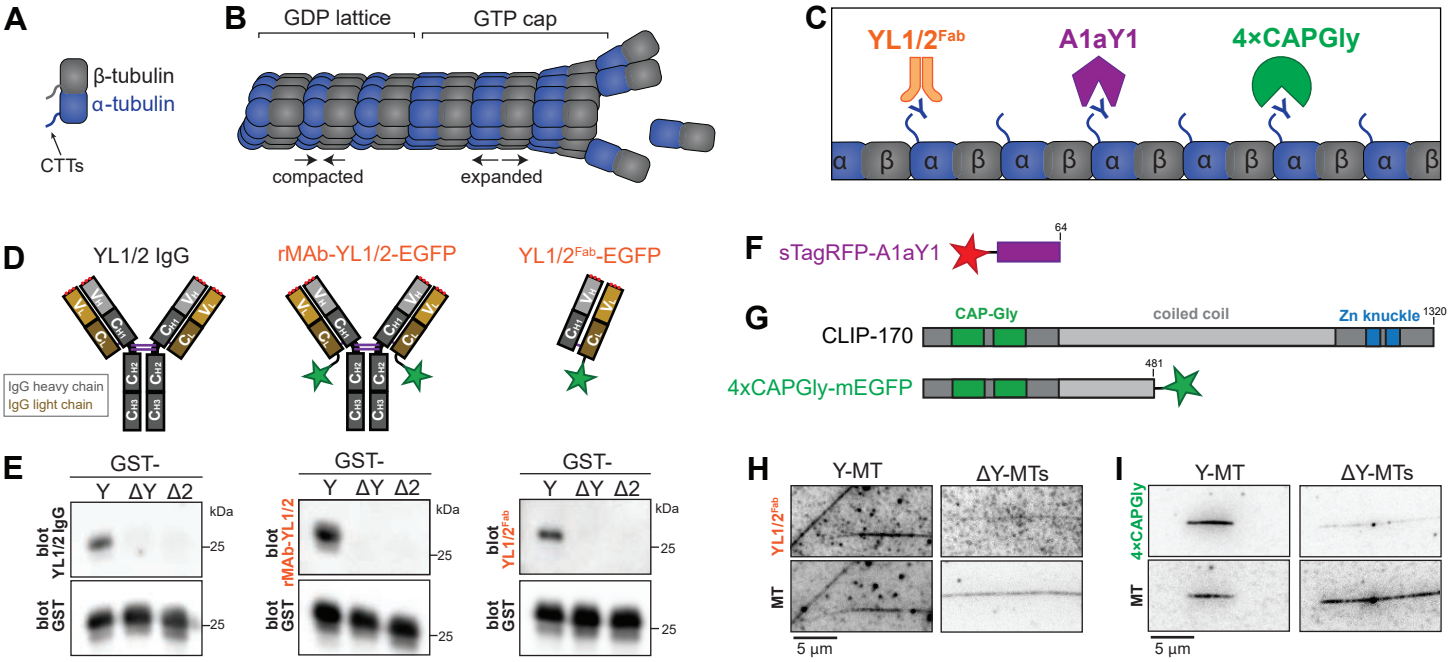
A
β-tubulin
α-tubulin
CTTs
B
GDP lattice
GTP cap
compacted
expanded
C
YL1/2Fab
A1aY1
4×CAPGly
α β α β α β α β α β α β α β
D
YL1/2 IgG
rMAb-YL1/2-EGFP
YL1/2Fab-EGFP
IgG heavy chain
IgG light chain
E
GST-
Y ΔY Δ2
kDa
25
blot YL1/2 IgG
blot rMAb-YL1/2
blot YL1/2Fab
blot GST
F
sTagRFP-A1aY1
64
G
CLIP-170
CAP-Gly
coiled coil
Zn knuckle
1320
4xCAPGly-mEGFP
481
H
Y-MT
ΔY-MTs
YL1/2Fab
MT
5 µm
I
Y-MT
ΔY-MTs
4×CAPGly
MT
5 µm

A

YL1/2 rat IgG sequence

Heavy chain gamma 2A (440 aa):

* * * * *

EVQVLESGGGLVQPGNSLKLSCATS GFTFSSA RMYWYRQFPEKRLEWVAR
I KAKSDNYA TDYTESVKGRFTISRDDSKSSIYLQMNNLKEEDTALYYCGW
FDSGYDY WGQGVMVTVSSAETTAPSVYPLAPGTALKSNSMVTLGCLVKGY
FPEPVTVTWNSGALSSGVHTFPAVLQSGLYTLTSSVTVPSSTWSSQAVTC
NVAHPASSTKVDKKIVPRECNPCGCTGSEVSSVFIFPPKTKDVLTITLTP
KVTCVVVDISQNDPEVRFSWFIDDVEVHTAQTHAPEKQSNSTLRSVSELP
IVHRDWLNGKTFKCKVNSGAFPAPIEKSISKPEGTPRGPQVYTMAPPKEE
MTQSQVSITCMVKGFYPPDIYTEWKMNGQPQENYKNTPPTMDTDGSYFLY
SKLNVKKETWQQGNTFTCSVLHEGLHNHHTEKSLSHSPGK

Light chain kappa (219 aa):

* * * * *

DIVLTQAPLSVSVTPGESASISC RSSKSLLRSKGITSLY WYLQRPGKSPQ
LLIY QMSNLASGVPDRFSSSGSETDFTLKISKVETEDVGVYYC GHRLEYP
PT FGGGTKLELKRADAAPTVSIFPPSTEQLATGGASVVCLMNNFYPRDIS
VKWKIDGTERRDGVLDSVTDQDSKDSTYSMSSTLSLTKADYESHNLYTCE
VVHKTSSSPVVKSFNRNEC

B

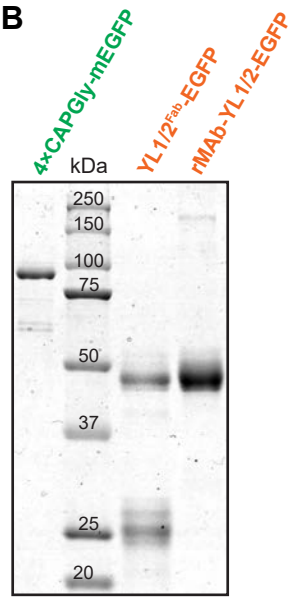

C

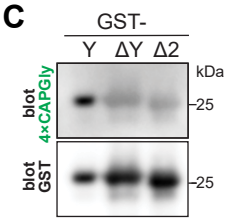

A. sTagRFP-A1aY1 co-expressed with mEGFP in COS-7 cells (imaged live)

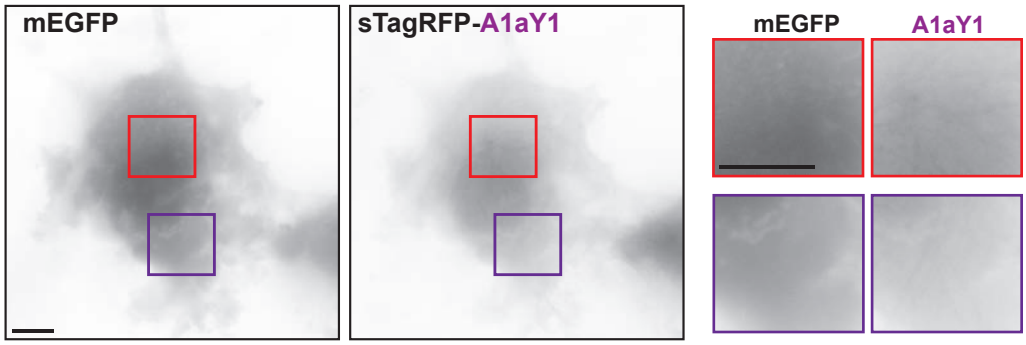

B. sTagRFP-A1aY1 co-expressed with mEGFP in COS-7 cells (fixed)

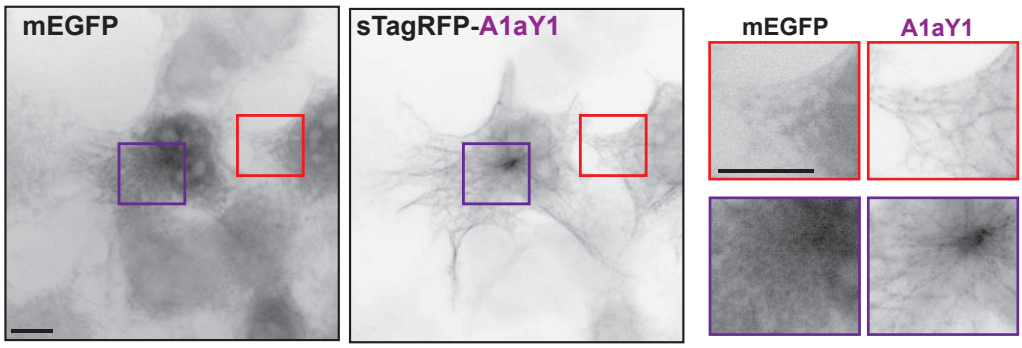

C. sTagRFP-A1aY1 co-expressed with mEGFP in COS-7 cells (fixed and stained for total tubulin)

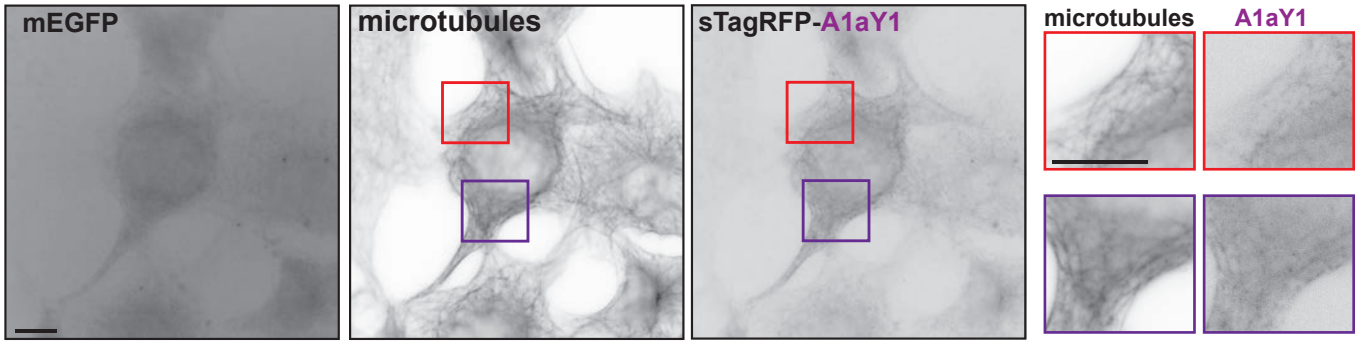

A. 4xCAPGly-mSc3 expressed with mEGFP in COS-7 cells (imaged live)

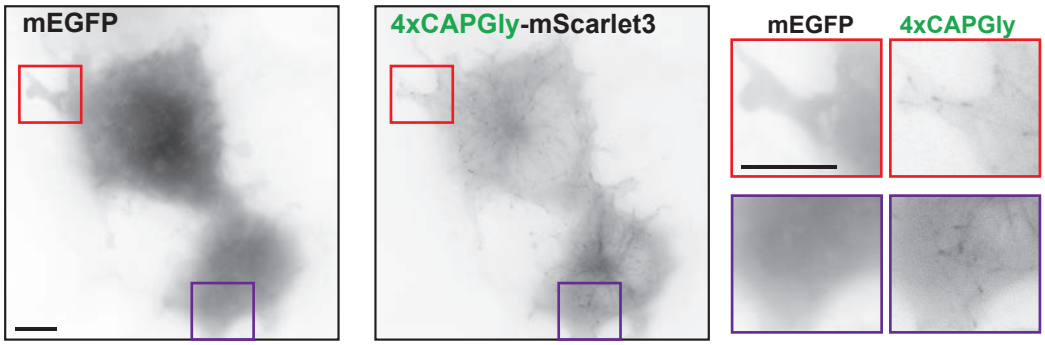

B. 4xCAPGly-mSc3 expressed with mEGFP in COS-7 cells (fix and mount)

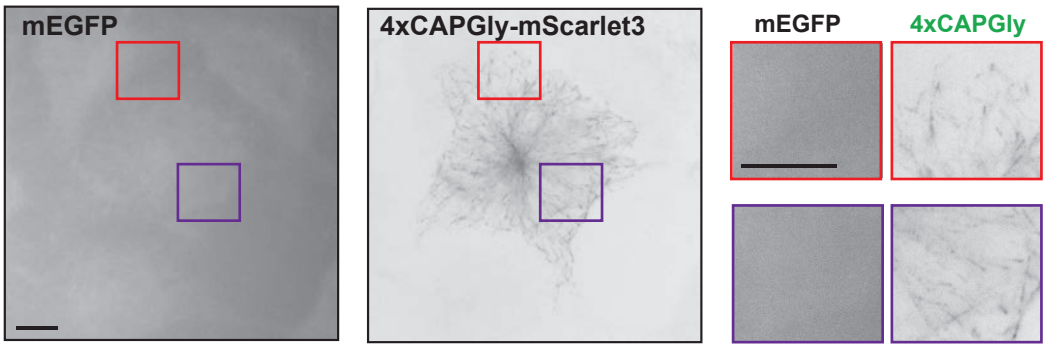

C. 4xCAPGly-mSc3 expressed with mEGFP in COS-7 cells (fixed and stained for total tubulin)

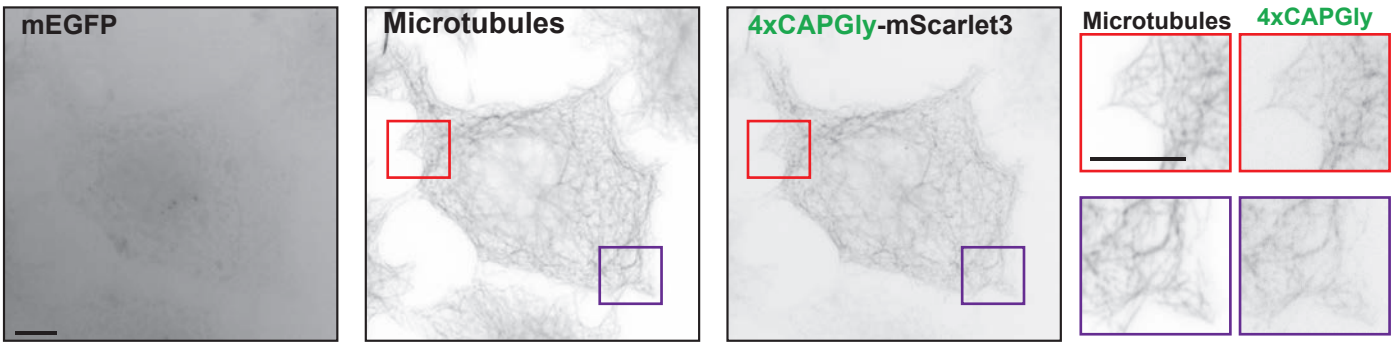

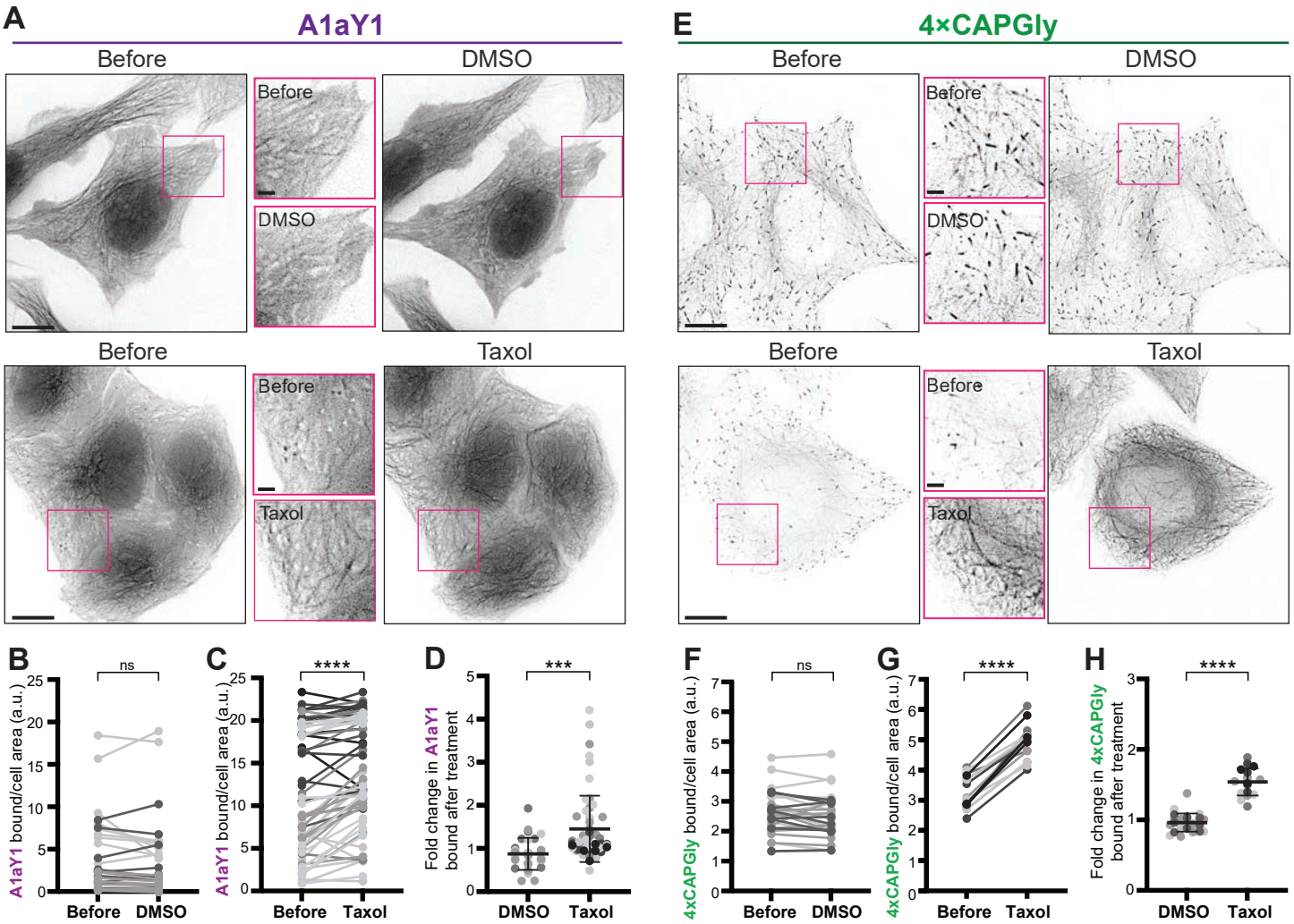
A
A1aY1
Before
DMSO
Before
DMSO
Before
Taxol
Before
Taxol
E
4×CAPGly
Before
DMSO
Before
DMSO
Before
Taxol
Before
Taxol
B
ns
A1aY1 bound/cell area (a.u.)
Before
DMSO
C
****
A1aY1 bound/cell area (a.u.)
Before
Taxol
D
***
Fold change in A1aY1 bound after treatment
DMSO
Taxol
F
ns
4xCAPGly bound/cell area (a.u.)
Before
DMSO
G
****
4xCAPGly bound/cell area (a.u.)
Before
Taxol
H
****
Fold change in 4xCAPGly bound after treatment
DMSO
Taxol

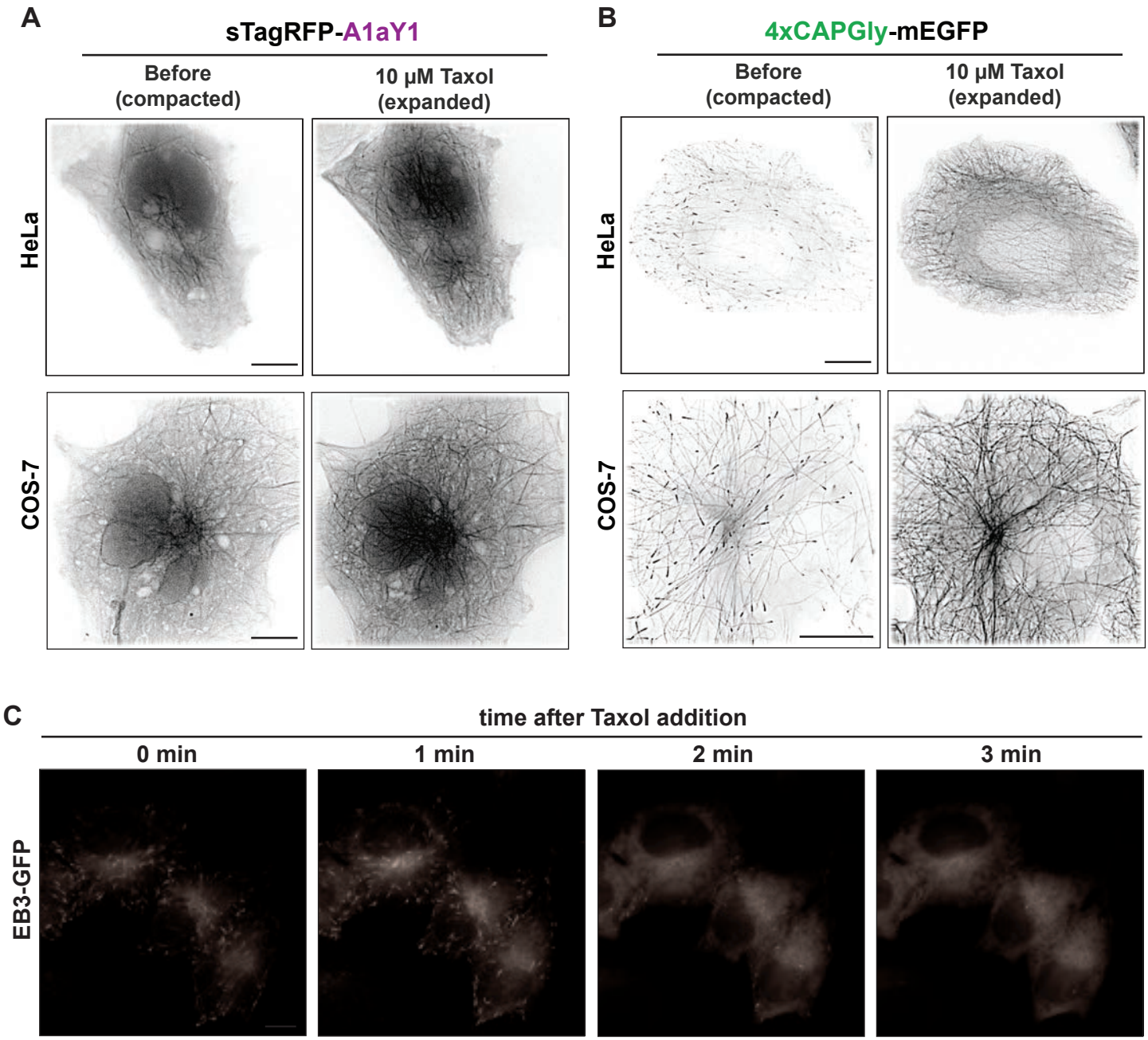
A
sTagRFP-A1aY1
Before (compacted)
10 μM Taxol (expanded)
HeLa
COS-7
B
4xCAPGly-mEGFP
Before (compacted)
10 μM Taxol (expanded)
HeLa
COS-7
C
time after Taxol addition
0 min
1 min
2 min
3 min
EB3-GFP

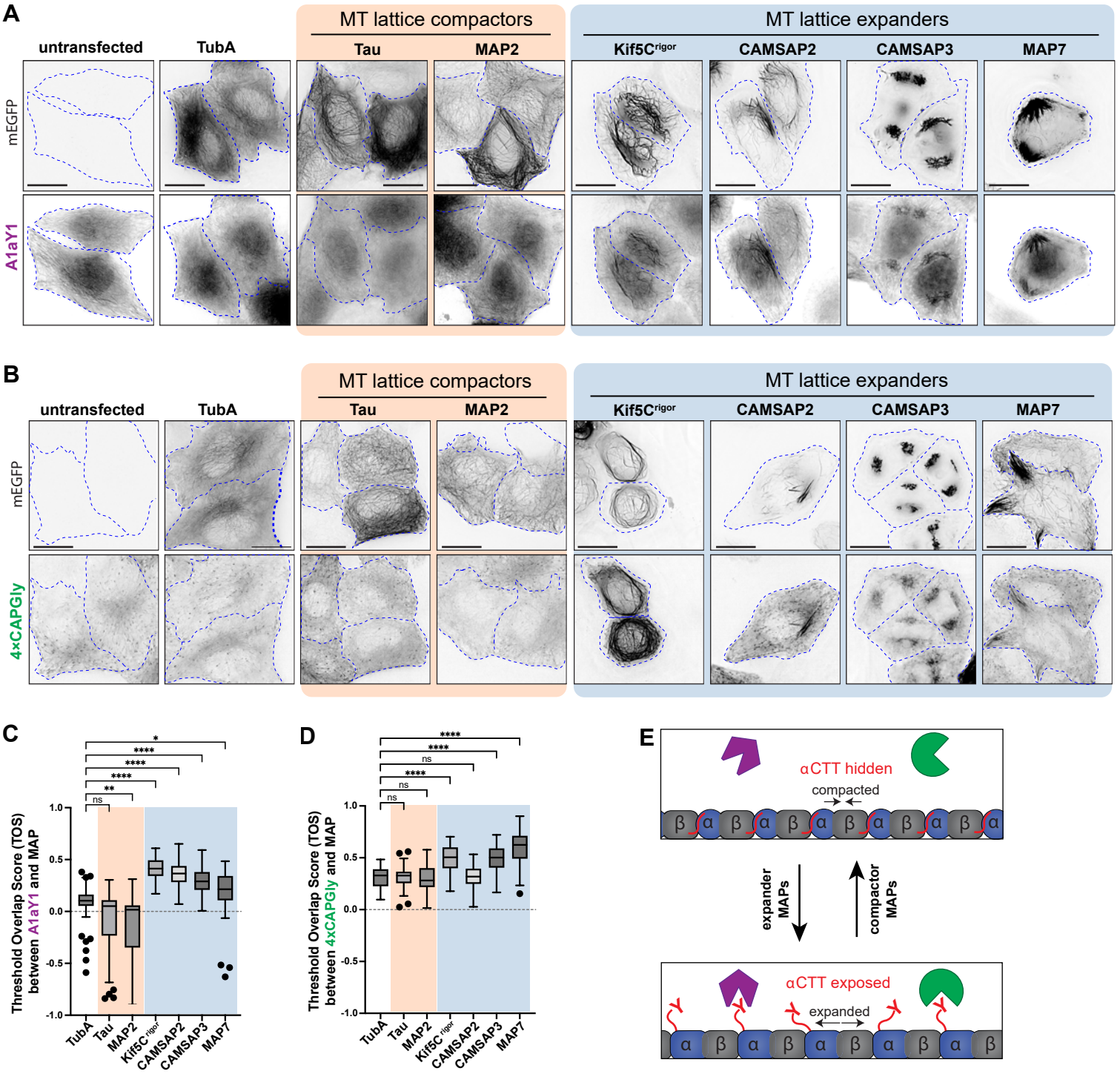
A
MT lattice compactors
MT lattice expanders
untransfected
TubA
Tau
MAP2
Kif5C rigor
CAMSAP2
CAMSAP3
MAP7
mEGFP
A1aY1
B
4xCAPGly
C
Threshold Overlap Score (TOS) between A1aY1 and MAP
D
Threshold Overlap Score (TOS) between 4xCAPGly and MAP
E
αCTT hidden
compacted
expander MAPs
compactor MAPs
αCTT exposed
expanded

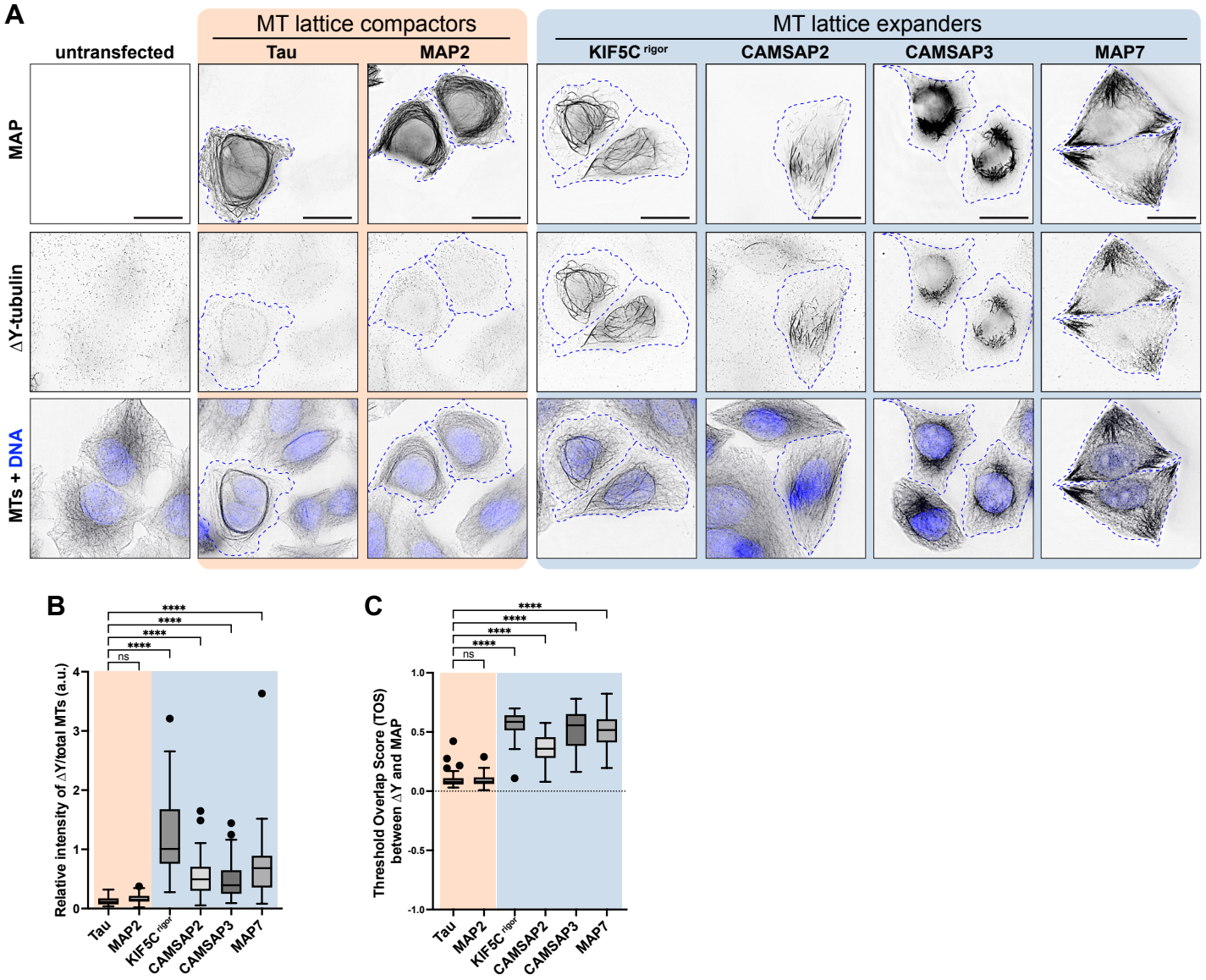
A
MT lattice compactors
MT lattice expanders
untransfected
Tau
MAP2
KIF5C rigor
CAMSAP2
CAMSAP3
MAP7
MAP
ΔY-tubulin
MTs + DNA
B
Relative intensity of ΔY/total MTs (a.u.)
****
ns
C
Threshold Overlap Score (TOS) between ΔY and MAP

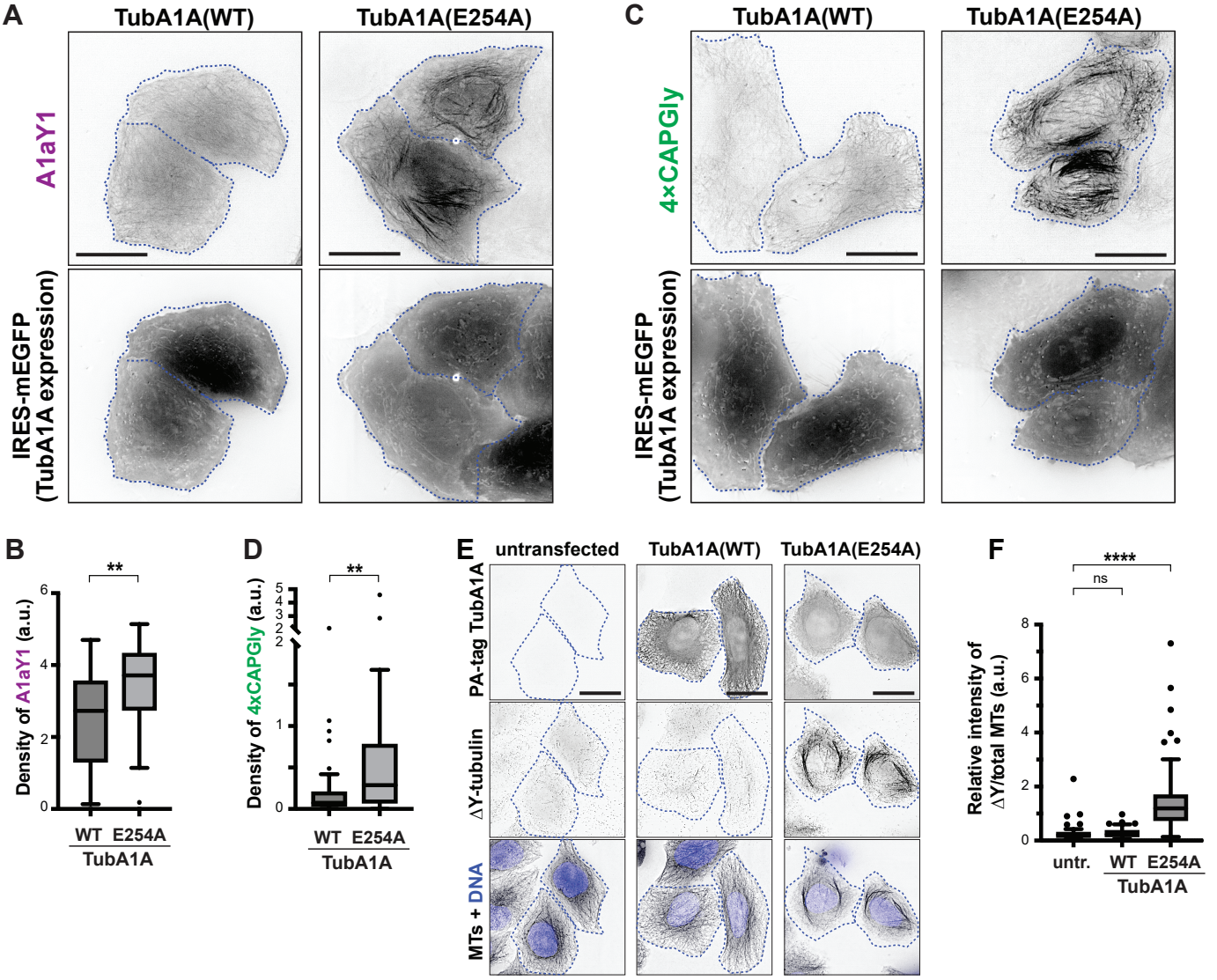
A
TubA1A(WT)
TubA1A(E254A)
A1aY1
IRES-mEGFP
(TubA1A expression)
C
TubA1A(WT)
TubA1A(E254A)
4×CAPGly
IRES-mEGFP
(TubA1A expression)
B
**
Density of A1aY1 (a.u.)
0
2
4
6
WT
E254A
TubA1A
D
**
Density of 4xCAPGly (a.u.)
0
1
2
3
4
5
WT
E254A
TubA1A
E
untransfected
TubA1A(WT)
TubA1A(E254A)
PA-tag TubA1A
ΔY-tubulin
MTs + DNA
F
****
ns
Relative intensity of
ΔY/total MTs (a.u.)
0
2
4
6
8
untr.
WT
E254A
TubA1A

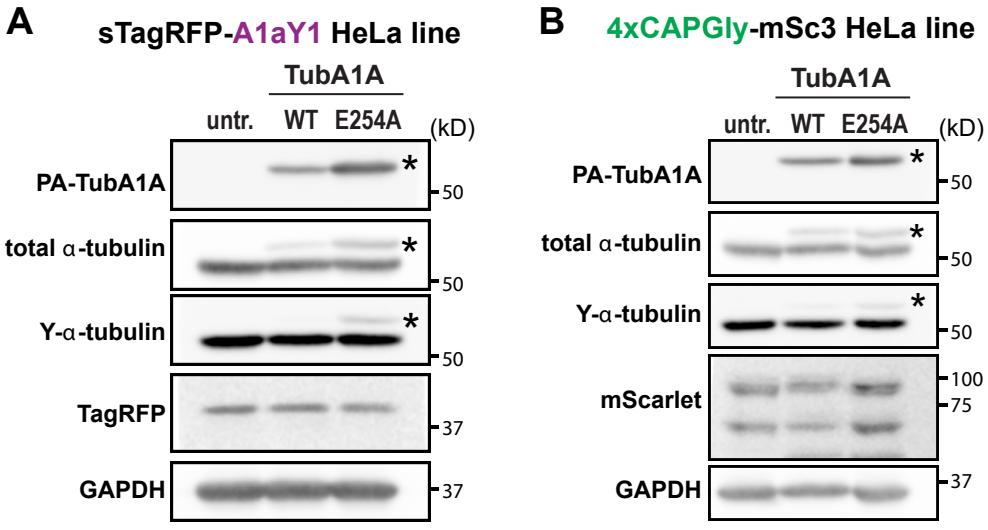
A
sTagRFP-A1aY1 HeLa line
TubA1A
untr.
WT
E254A
(kD)
PA-TubA1A
total α-tubulin
Y-α-tubulin
TagRFP
GAPDH
50
50
50
37
37
B
4xCAPGly-mSc3 HeLa line
TubA1A
untr.
WT
E254A
(kD)
PA-TubA1A
total α-tubulin
Y-α-tubulin
mScarlet
GAPDH
50
50
50
100
75
37

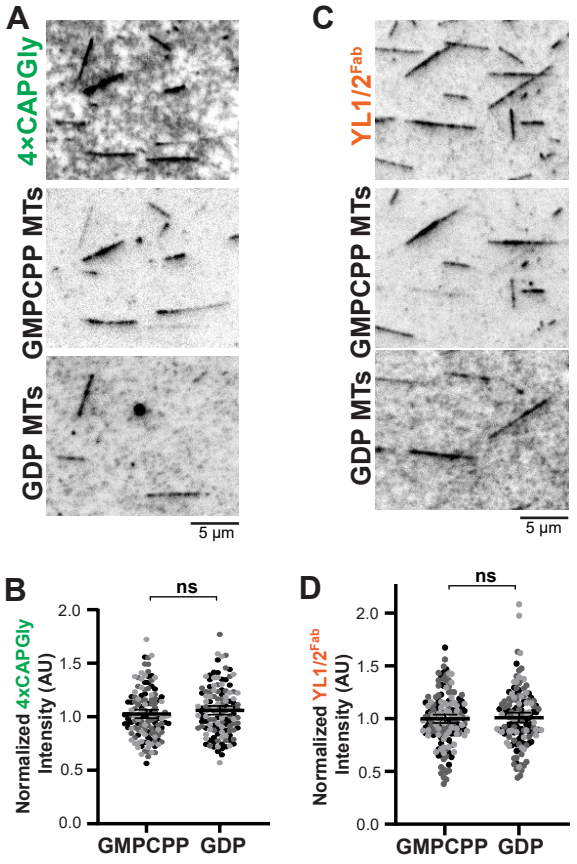
A
4×CAPGly
GMPCPP MTs
GDP MTs
5 µm
C
YL1/2Fab
GMPCPP MTs
GDP MTs
5 µm
B
ns
Normalized 4xCAPGly Intensity (AU)
2.0
1.5
1.0
0.5
0.0
GMPCPP
GDP
D
ns
Normalized YL1/2Fab Intensity (AU)
2.0
1.5
1.0
0.5
0.0
GMPCPP
GDP

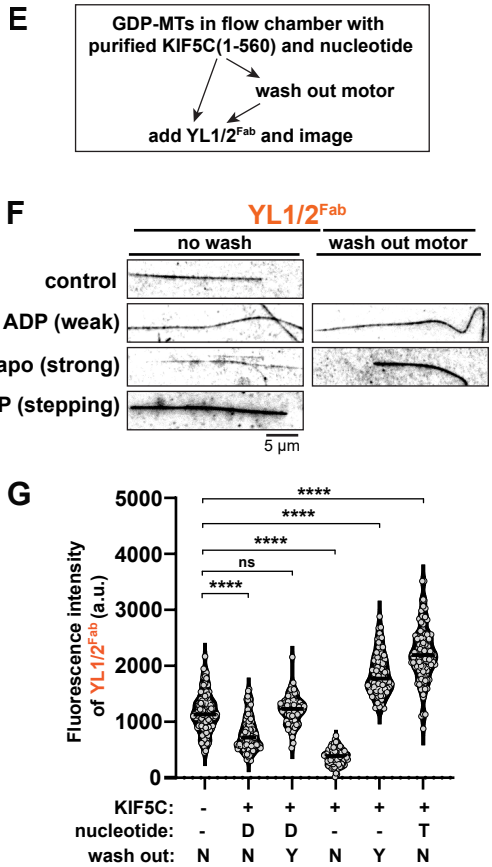
E
GDP-MTs in flow chamber with purified KIF5C(1-560) and nucleotide
wash out motor
add YL1/2Fab and image
F
YL1/2Fab
no wash
wash out motor
control
KIF5C
ADP (weak)
apo (strong)
ATP (stepping)
5 µm
G
Fluorescence intensity of YL1/2Fab (a.u.)
5000
4000
3000
2000
1000
0
****
****
****
ns
****
KIF5C: - + + + + +
nucleotide: - D D - - T
wash out: N N Y N Y N

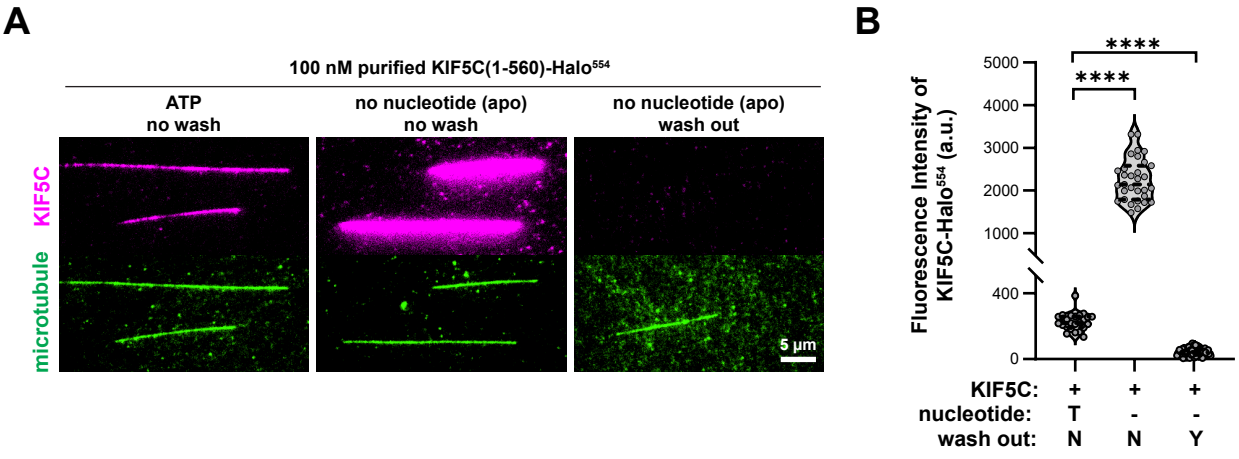
A
100 nM purified KIF5C(1-560)-Halo554
ATP
no wash
no nucleotide (apo)
no wash
no nucleotide (apo)
wash out
KIF5C
microtubule
5 µm
B
Fluorescence Intensity of KIF5C-Halo554 (a.u.)
5000
4000
3000
2000
1000
400
0
****
****
KIF5C: + + +
nucleotide: T - -
wash out: N N Y

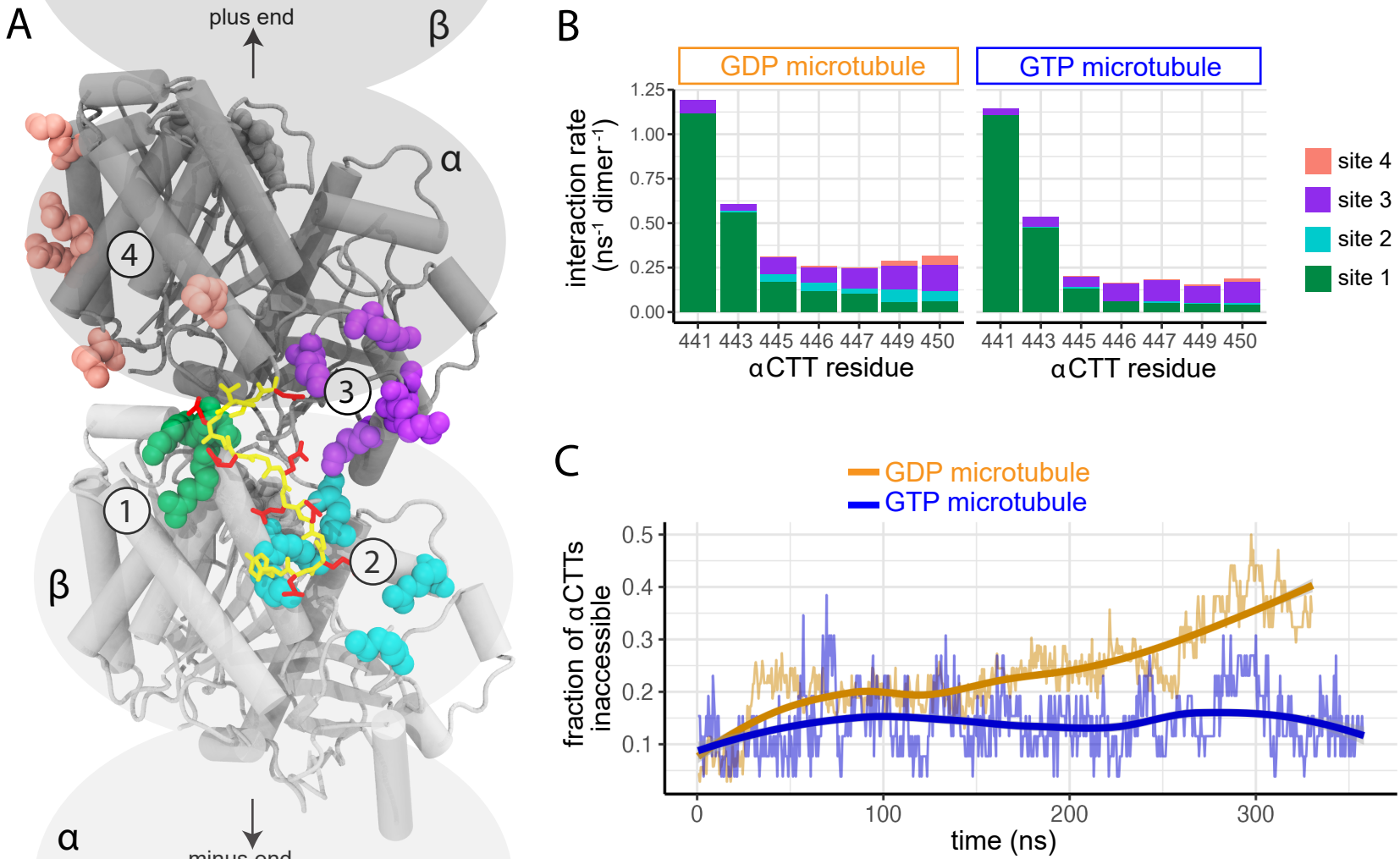
A
plus end
β
α
4
3
1
2
β
α
minus end
B
GDP microtubule
GTP microtubule
interaction rate (ns⁻¹ dimer⁻¹)
1.25
1.00
0.75
0.50
0.25
0.00
441 443 445 446 447 449 450
αCTT residue
441 443 445 446 447 449 450
αCTT residue
site 4
site 3
site 2
site 1
C
GDP microtubule
GTP microtubule
fraction of αCTTs inaccessible
0.5
0.4
0.3
0.2
0.1
0
100
200
300
time (ns)

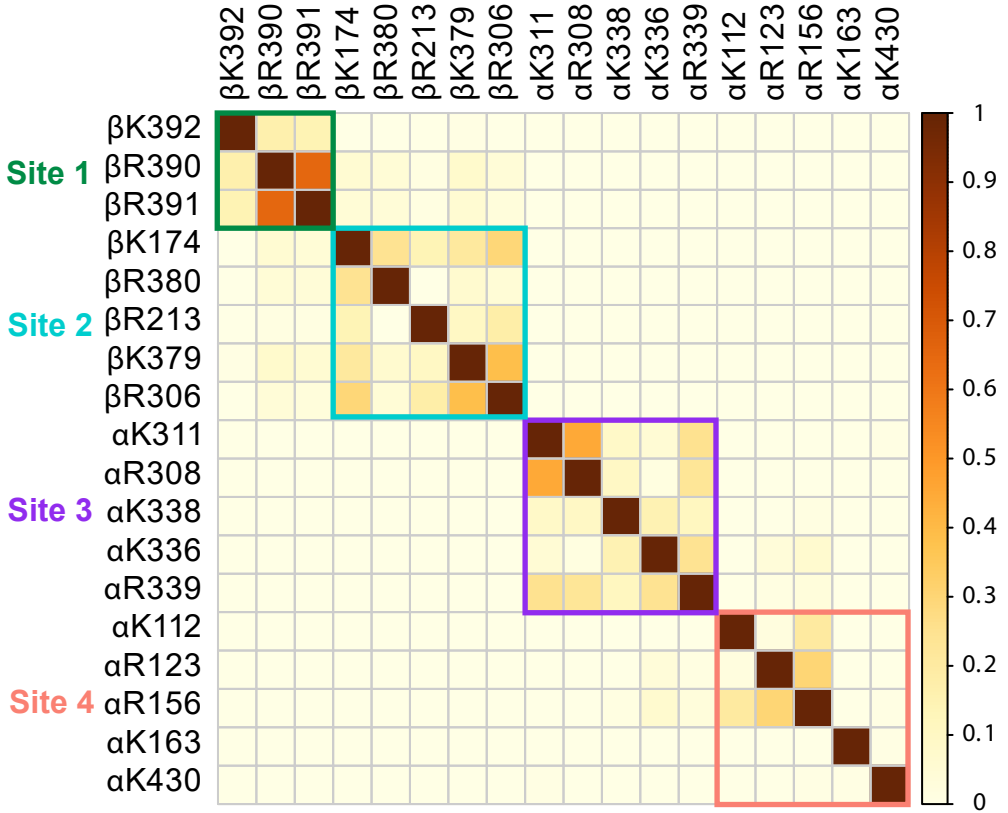
βK392
βR390
βR391
βK174
βR380
βR213
βK379
βR306
αK311
αR308
αK338
αK336
αR339
αK112
αR123
αR156
αK163
αK430
Site 1
Site 2
Site 3
Site 4
1
0.9
0.8
0.7
0.6
0.5
0.4
0.3
0.2
0.1
0